AMERICAN UNIVERSITY OF BEIRUT

ADAPTIVE CONTROLLER DESIGN of MRI COMPATIBLE PNEUMATIC TELEOPERATION SYSTEM

by
MOHAMAD ANWAR BAAYOUN

A thesis
submitted in partial fulfillment of the requirements
for the degree of Master of Engineering
to the Department of Mechanical Engineering
of the Faculty of Engineering and Architecture
at the American University of Beirut

Beirut, Lebanon
September 2015

AMERICAN UNIVERSITY OF BEIRUT

ADAPTIVE CONTROLLER DESIGN of MRI COMPATIBLE
PNEUMATIC TELEOPERATION SYSTEM

by
MOHAMAD ANWAR BAAYOUN

Approved by:

_____

Dr. Matthias Liermann, Assistant Professor   Advisor

Mechanical Engineering

_____

Dr. Naseem Daher, Assistant Professor   Member of Committee

Electrical and Computer Engineering and Mechanical Engineering

_____

Dr. Elie Shammas, Assistant Professor   Member of Committee

Mechanical Engineering

Date of thesis defense: September 14, 2015

AMERICAN UNIVERSITY OF BEIRUT

THESIS, DISSERTATION, PROJECT RELEASE FORM

Student Name: __Baayoun_____Mohamad_____Anwar___
                Last   First   Middle

◯ Master's Thesis   ◯ Master's Project   ◯ Doctoral Dissertation

☑   I authorize the American University of Beirut to: (a) reproduce hard or electronic copies of my thesis, dissertation, or project; (b) include such copies in the archives and digital repositories of the University; and (c) make freely available such copies to third parties for research or educational purposes.

☐   I authorize the American University of Beirut, **three years after the date of submitting my thesis, dissertation, or project,** to: (a) reproduce hard or electronic copies of it; (b) include such copies in the archives and digital repositories of the University; and (c) make freely available such copies to third parties for research or educational purposes.

_____   ___28/9/2015___
Signature   Date

Acknowledgements

An Abstract of the Thesis of

Mohamad Anwar Baayoun   for   Master of Engineering
                                                Major: Mechanical Engineering

Title: Adaptive Controller Design Of MRI Compatible Pneumatic Teleoperation System

This work presents an adaptive control design of a pneumatic teleoperation system that could be useful for applications like MRI-guided surgery. The system under study is unique because of its reduced number of components compared to other bilateral teleoperation systems, so cost and complexity are reduced. The direct fluidic connection and force feedback that is transferred to the human operator allow the operator to feel as if s/he were having physical contact with the environment situated in another room without the need for a force sensor on the slave actuator. The system under study is implemented in simulation first, transparency and stability were assessed for different operating scenarios, and sensitivity study is conducted to investigate what parameters affect the system performance. A linear controller is optimized for various operating remote environments via frequency response analysis, and yielded satisfactory results for certain operating physical environments, but its tuning is dependent on the impedance characteristic of the environments both on the master and slave sides. Since the system must perform under parametric uncertainties on both sides of the teleoperator, an adaptive control scheme is developed. A self-tuning regulator is designed to allow the teleoperator to cope with variable operating conditions. Using recursive least-square estimation, system parameters are estimated continuously and the controller drives the system output to the commanded input using a specified reference model using pole placement, so it can adapt to any change in environment impedances on both sides of the teleoperator. The controller is validated both in simulation and experiment, and yielded satisfactory performance under multiple operating conditions.

Keywords: Teleoperation system, adaptive control, lead compensator, pneumatic actuator, self tuning regulator, pipeline dynamics.

Contents

List of Figures

List of Tables

Chapter 1

Introduction

Teleoperators are used in situations where the human operator cannot have physical interaction with the remote environment, so they allow the human operator to control an actuator remotely.

Teleoperation systems are generally composed of a master and a slave, as shown in Figure (1.1), and use a specific communication scheme between these two to achieve the required goal of allowing the operator to interact with the physical environment remotely [1].

In some situations, the human operator cannot have direct contact with the task environment due to several reasons: geometric and physical constraints, danger on human life, human operator and environment location, etc.
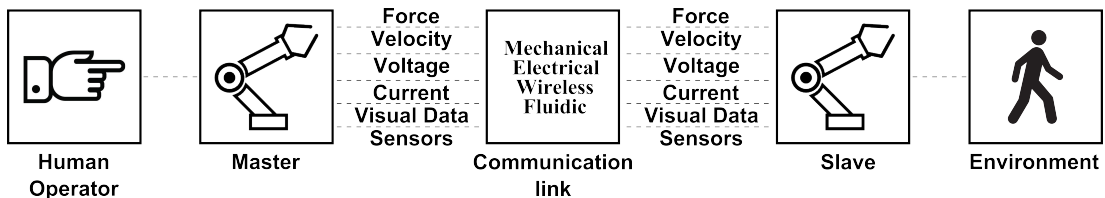
Figure 1.1: General teleoperation system composition

If the slave reflects force from the task environment to the human operator, the teleoperator is said to be controlled bilaterally [2]. Advances were done in this field using different actuation techniques and different communication protocols like mechanical, electrical, wireless or fluidic, for different applications such as medical, nuclear or marine. These advances tend to improve two important criteria that define the performance of the teleoperator, stability and transparency.

In network theory, n-port system is characterized by the relationship between effort and flow [3]. The effort f can be the force output of a mechanical system, or the voltage output of an electrical system; the flow v can be the velocity input of a mechanical system or the current input of an electrical system. For a linear time-invariant, lumped one-port network, the relationship is denoted as impedance $Z(s)$, which is the ratio

1
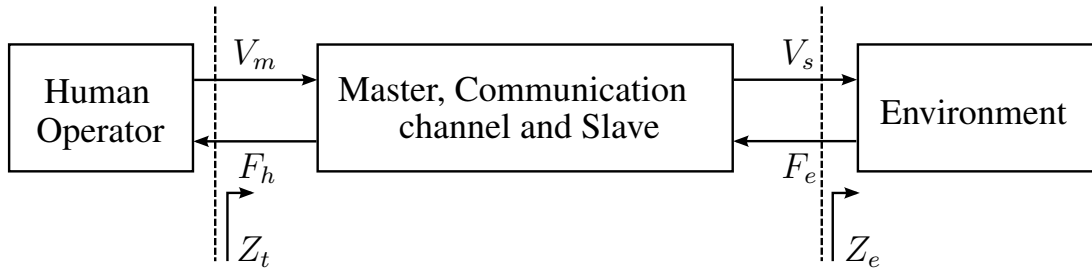
Figure 1.2: Transparency assessment evaluated impedances Z_t and Z_e

between effort f and flow v:

$$Z(s) = \frac{f(s)}{v(s)} \tag{1.1}$$

where $f(s)$ and $v(s)$ are the Laplace transforms of f and v, respectively. Figure (1.2) shows the different parameters communicated between the master and slave actuators, where V_m is the velocity of the human operator hand and F_h is the force transferred from the teleoperator. V_s and F_e are the velocity of the slave actuator and force reflected by the environment, respectively.

Transparency is defined as the impedance ratio between the master and the slave:

$$\text{Transparency} = \frac{Z_t}{Z_e} \tag{1.2}$$

Z_t is the impedance of the teleoperator system including the environment impedance, it is given by:

$$Z_t = \frac{F_h}{V_m} \tag{1.3}$$

Z_e is the environment impedance, it is given by:

$$Z_e = \frac{F_e}{V_s} \tag{1.4}$$

The goal of a teleoperator is to make the impedance felt by the operator Z_t equal to the actual environment impedance Z_e. The system stability is influenced by both operator and environment dynamics [4]. Stability and transparency are two conflicting design issues [5] . A good teleoperator design is the one that can accomplish a good tradeoff between stability and transparency. This tradeoff is based on many assumptions: application, accuracy needed, environment and operator behavior, etc.
Pneumatic actuators are widely used in teleoperation systems due to a variety of benefits over other types of actuation: low cost, backdrivability, ease of implementation, precision sensing and high force to weight ratio. In this research, the purpose is to assess and control a 1 degree of freedom pneumatic actuator with force feedback to be implemented and used under real-time MRI imaging. The teleoperation system was

first presented in [6]. Initial testing of the system identified the challenge of optimizing transparency while maintaining stability.

This research started by first analyzing what has been done in literature regarding pneumatic teleoperator systems, establishing architecture of the system in comparison to Lawrence [5], implementation in simulation, assessing transparency and stability, optimizing linear control design, and developting an adaptive controller capable of improving system transparency while maintaining stability so that the system is capable to operate under variable operating conditions.

Chapter 2 presents a literature review of the topic, chapter 3 states the governing equations of the model, chapter 4 presents transparency assessment of the present system, chapter 5 introduces the designed linear controller with simulation results, chapter 6 presents the adaptive control design tested in simulation with transparency assessment, chapter 7 presents the system performance applying the proportional, lead compensator and adaptive controllers in 2 different operating environments, with different human operator behavior, both in simulation and experiment. Chapter 8 concludes the work.

Chapter 2

Literature Review

To investigate the different methods used by previous researches to control and optimize teleoperators performance in terms of stability and transparency, a literature review was conducted. Different approaches were used to solve this problem, each researcher tried to solve it by proposing a certain methodology to follow based on his system's performance and capabilities. Dale A. Lawrence presented in [5] a general multivariable architecture that can be used in bilateral teleoperation systems as shown in Figure (2.1), where F_h and F_e are the forces acting on the master and slave actuators respectively. The reflection of force F_h by the hand caused from motion V_h of the slave actuator is characterized by the hand-arm impedance Z_h. An additional exogenous force F_h^* can be exerted by the operator to move the master cylinder to its desired position. Similarly, the reflection of force from the environment caused from slave actuator motion is characterized by the environment impedance Z_e. Also the environment may have an active component that causes an exogenous force F_e^*. C_1, C_2, C_3, C_4, C_s and C_m are communication links defined in [5]. The architecture is transmitting four variables, force and velocity in both directions (master and slave). This architecture was the source of many papers published in the last two decades, where researchers optimized design for better teleoperators behavior.
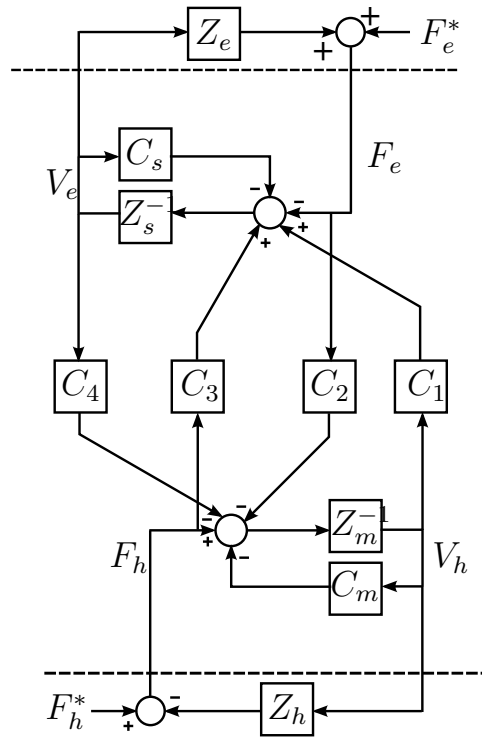
Figure 2.1: Bilateral teleoperation architecture done by Lawrence [5]

Building teleoperation systems that are under rate control or more generalized master-slave correspondence laws was done in [3], such as mixed position-rate mode. The paper started from Lawrence's architecture [5], and built a more general structure that can be used in bilateral teleoperators, which provides better force feedback to the operator. General analysis of performance and stability robustness of impedance-impedance 3-channel architectures was presented in [7]. The analysis was targeted for tele-surgery applications on soft tissue, where relatively low frequencies are used, negligible time delay and low impedances exist. The paper recommended using the Position, Position-Force architecture based on analysis of simulation evaluation results.

Literature shows that using kinesthetic force feedback in passive teleoperator systems, which enhances the operator feeling in the environment force, improves transparency, so the human operator feels exactly as if s/he is having physical contact with the environment. However, stability is not guaranteed under all conditions. On the other hand, using cutaneous force feedback (which helps identifying the properties and features of the environment) leads to good stability but less transparent systems [8]. Combining cutaneous and kinesthetic force feedback in teleoperators was presented in [8], where force feedback is computed on the master side and is actuated via a kinesthetic device, as long as the passivity condition is not violated. When the passivity layer detects a violation and the kinesthetic device is unable to provide the required feedback, a cu-

taneous actuator conveys a suitable tactile sensation according to the amount of force, while recovering transparency.

Combining visual and haptic feedback on computer-assisted needle insertion was tested in [9]. It presented improved performance especially in cases where low stiffness tissues were present. Real-time visual feedback enhances controlled puncture in needle insertion. The force feedback importance increases when visual feedback is limited or when sudden release of force occurs on the environment side.

Environment parameter estimation architecture was presented in [10] where nonlinear stiffness and damping of the physical environment are estimated using indirect adaptive control approach, which improved transparency, gave realistic results, and allowed the controller to provide the necessary information from the remote environment to the human operator.

A model-based adaptive controller was designed for Pneu-WREX robot for rehabilitation in [11], a novel kalman filter is developed for state estimation. Flow dynamics of air and leakage were estimated to be included in Lyapunov analysis (experimental data was used to characterize the used servovalve).

A novel idea of pneumatic robot for transperineal prostate needle placement for biopsy and brachytherapy seed placement is presented in [12]. The mechanism design fits with the geometrical constraints of the scanner and in the same time guarantees the required motion specified by the operator (which was limited to 2 DOF: vertical and horizontal). Using sliding mode control (SMC) to actuate and control the piezoelectrically actuated valves that are situated near the patient, the system was tested and validated under live MR imaging regarding MR compatibility, workspace and workflow and localization and placement accuracies.

The design, implementation and evaluation of a pneumatic actuated robotic assistant system for real time MRI guided aortic valve replacement is presented in [13]. The system integrates real time MRI with the robotic arm and the new developed valve delivery module VDM. The system is MRI compatible, the signal to noise ratio of the imaging was 8.2 % with the presence and motion of the robotic arm inside the scanner. Using PIV (proportional position loop integral and proportional velocity) controller, the system presented perfect tracking of the command in continuous mode with minimal position and velocity errors.

As a summary of what was presented in literature, optimizing transparency was done in different ways:

1. Improving the architecture, i.e changing communication lines and transferred variables [5, 3, 7].

2. Choice of sensors, and improving sensors design [8].

3. Proper choice of controller type [10, 11, 12, 13]

Improving the controller is a suitable solution to improve teleoperator performance, controller choice and design play a major role in defining system's performance. This choice will be developed in next chapters of this thesis.

Chapter 3

System Model

This chapter introduces the governing equations of the model. Figure (3.1) shows the different physical components of the system, and how they are connected. Master and slave actuators are connected with a physical connection, i.e. pneumatic lines. Two position sensors are connected to the pistons, and two pressure sensors are connected to the tubes. The valves are placed near the master actuator and are used by the controller to adjust the pressures in the lines connecting master and slave cylinders.

3.1 Nonlinear System Model

The model equations are divided into four main parts: actuators motion, cylinder chamber pressure drop, valve dynamics and tube model.

3.1.1 Actuator Motion

The force transmitted to the human operator is given by:

$$F_h = (P_{m1} - P_{m2})A_p - m_p\ddot{x}_m - \beta\dot{x}_m \tag{3.1}$$

where P_{m1} and P_{m2} are the pressures of chamber 1 and 2 of the master cylinder, A_p is the cross sectional area of the piston, x_m is the master piston position, β is the viscous friction coefficient of the pistons and m_p is the mass of the piston. The slave piston equation of motion is given by:

$$m_p\ddot{x}_s + \beta\dot{x}_s = (P_{s1} - P_{s2})A_p - B_e\dot{x}_s - K_e x_s \tag{3.2}$$

where P_{s1} and P_{s2} are the pressures of chamber 1 and 2 of the slave cylinder, x_s is the slave piston position, B_e is the damping coefficient and K_e is the spring constant of the environment model.
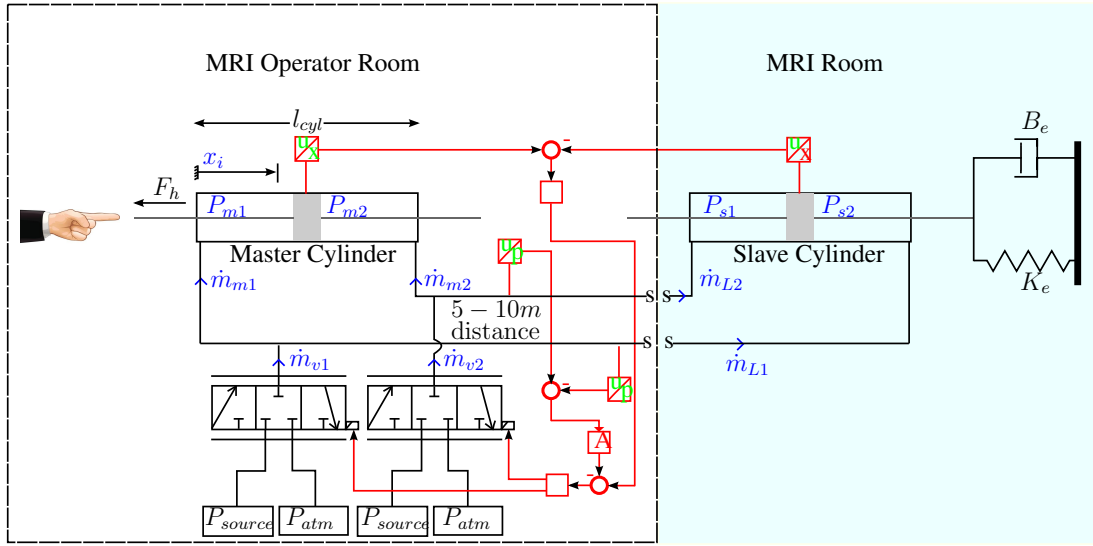
Figure 3.1: Pneumatic teleoperation system schematic (Pneumatic connection in black, electrical connection in red)

3.1.2 Cylinder Chamber Pressure Drop

Figure (3.2) shows the cylinder model, indicating pressures in each chamber, mass flow rates and piston position reference. Assuming isothermal conditions because we
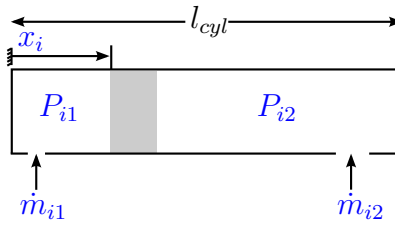
Figure 3.2: Flow rate in each chamber of the cylinder

don't expect fast movements in the teleoperation application, the rate of change of the pressure in chamber 1 of each cylinder is given by:

$$\dot{P}_{i1} = \frac{RT}{V_{i1}}\dot{m}_{i1} - \frac{P_{i1}}{V_{i1}}\dot{V}_{i1} \tag{3.3}$$

where $i = m$ or s refers to either master or slave respectively, P_{i1} is the pressure in chamber 1 in each cylinder, V_{i1} is the volume of chamber 1 in each cylinder.

With the volume of chamber 1 written in terms of cylinder position:

$$V_{i1} = V_{id} + x_i A_p \tag{3.4}$$

8

where V_{id} is the dead volume of the chamber. Substituting Eq. (3.4), Eq. (3.3) becomes,

$$\dot{P}_{i1} = \frac{RT}{V_{id} + x_i A_p}\dot{m}_{i1} - \frac{P_{i1}}{V_{id} + x_i A_p}\dot{x}_i A_p \tag{3.5}$$

Similarly, the change in pressure in chamber 2 is expressed as,

$$\begin{aligned}
\dot{P}_{i2} &= \frac{RT}{V_{i2}}\dot{m}_{i2} - \frac{P_{i2}}{V_{i2}}\dot{V}_{i2} \\
&= \frac{RT}{V_{id} + (l_{cyl} - x_i)A_p}\dot{m}_{i2} + \frac{P_{i2}}{V_{id} + (l_{cyl} - x_i)A_p}\dot{x}_i A_p
\end{aligned} \tag{3.6}$$

3.1.3 Valve Dynamics

The valve is connected to the pressure supply and to the atmospheric pressure as shown in Figure (3.3), where the spool position x_v is controlled with the control input u. The
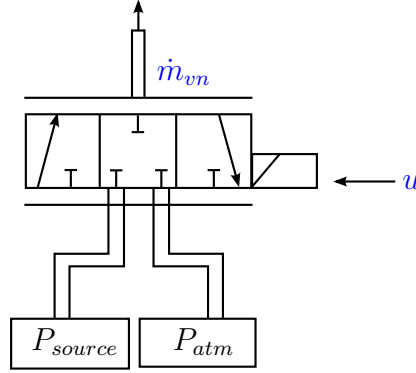
Figure 3.3: Valve Output Mass Flow Rate

mass influx of the valve $\dot{m}_{vn}$, related to the control input u, is given by ISO 6358 technical nozzles and orifices [14] as:

$$\dot{m}_{vn} = \begin{cases} u\,c\,\rho_0 P_{un}\sqrt{\frac{T_0}{T_{1n}}}\sqrt{1 - (\frac{\frac{P_{dn}}{P_{un}} - b}{1-b})^2} & \text{for } \frac{P_{dn}}{P_{un}} > b \\ u\,c\,\rho_0 P_{un}\sqrt{\frac{T_0}{T_{1n}}} & \text{for } \frac{P_{dn}}{P_{un}} \leqslant b \end{cases}$$

Where $n = 1$ or 2 refers to valve 1 or 2, c is the sonic conductance given by the valve manufacturer, ρ_0 is the density of air at reference conditions, P_{un} is the upstream pressure, T_0 is the temperature of air at reference conditions, T_{1n} is the upstream temperature of air, P_{dn} is the downstream pressure, and b is the critical pressure ratio given by the valve manufacturer.

The natural frequency of the valve spool position control is 400 Hz. Since this is fast compared to other dynamics in the system, it can be neglected for the purpose of control design.

9

3.1.4 Tube Modeling

Applying the conservation of mass and continuity equations for the lines, see figure (3.4), we get:

$$\dot{m}_{vn} = \dot{m}_{mn} + \dot{m}_{Ln} \tag{3.7}$$
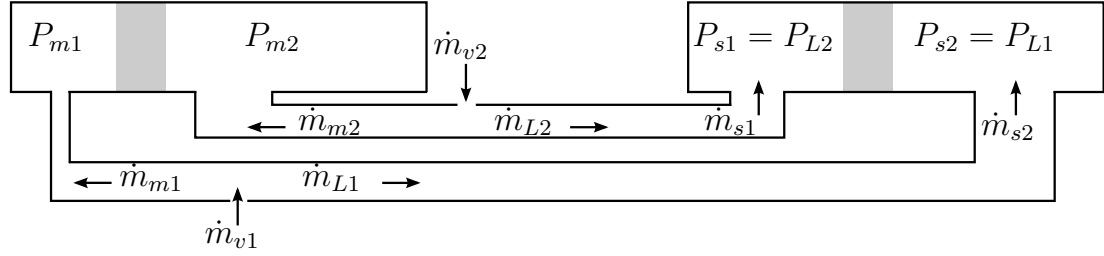
Figure 3.4: Mass flow rates and pressure change in pneumatic lines

Tube dynamics are modeled by a simplified equation, assuming the temperature change in and out of the lines is minimal, which is valid if the highest frequency f in rad/s follows the condition [14]:

$$f \leqslant \frac{4v}{A} \tag{3.8}$$

where v is the kinematic viscosity, and A is the cross sectional area of the lines. If this condition is satisfied, the tubes can be modeled with one or more elements with simple resistance, capacitance and inertance characteristic [15], as shown in Figure (3.5).
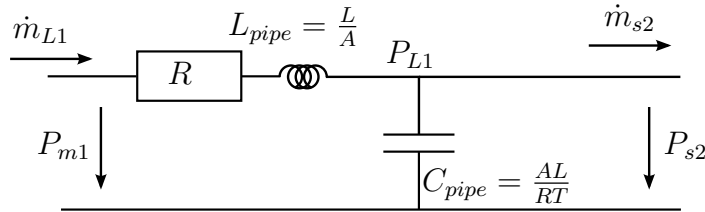
Figure 3.5: Tube model

The pressure gradient in the first line is given by:

$$\dot{P}_{L1} = \frac{RT}{AL}(\dot{m}_{L1} - \dot{m}_{s2}) \tag{3.9}$$

The mass flow rate is given by:

$$\frac{d\dot{m}_{L1}}{dt} = \frac{A}{L}(P_{m1} - P_{L1}) - \frac{A}{L}\Delta p_{friction} \tag{3.10}$$

The pressure loss for laminar flow is given by:

$$\Delta P_{friction} = \frac{32\mu\bar{w}L}{D^2} = \frac{32\mu\dot{m}_{L1}L}{\rho AD^2} \tag{3.11}$$

10

Finally, since the capacitance of the line is connected to the chamber of the cylinder, the following condition holds:

$$P_{L1} = P_{s2} \tag{3.12}$$

The model architecture is presented in Figure (3.6). The human operator hand force is considered as input to the master cylinder, which returns force feedback to the operator. The pressure drop caused by master cylinder movement is transferred
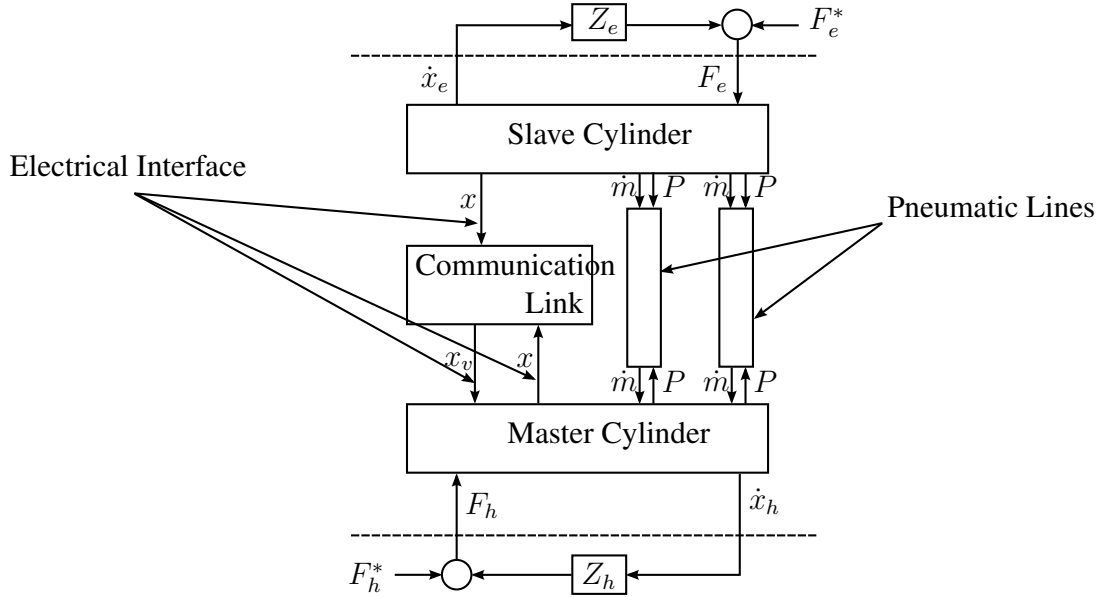
Figure 3.6: Proposed pneumatic teleoperation architecture

through the pneumatic lines from the master to the slave actuator to cause slave piston movement. On the other side, the environment force acting on the slave actuator is represented as the product of the environment impedance multiplied by the slave cylinder's velocity. What makes this architecture different than previous work is that the whole teleoperation system is one physical unit (master - lines - slave). It does not consist of two physically independent master and slave actuators that are only connected through control signals, compare Figure (2.1). This results in the fact that only one control signal (the valve spool position at master side) exists, while the architecture of Lawrence [5] has four control channels between master and slave.

3.2   Linearized Model Equations

A linearized model of the system is helpful in transparency assessment, the effect of changing geometry or control parameters on the behavior of the system is easily detected with the bode plot of the transparency ratio. This model is also helpful for linear control design, and it allows to determine the dominant subsystems for model reduction.

11

3.2.1 Linearized Pressure Dynamic Equations

Linearization of all system variables is done around an equilibrium point [6]. Using "~" above a state space value means that we consider the difference between the variable and its value at equilibrium (when the piston is in middle position of the cylinder and not moving). The equilibrium pressure in cylinder chambers is chosen in such a way between supply and atmospheric pressure that the system responds symmetrically for positive and negative valve openings for positive and negative mass flow of the valves [6]. From equations (3.3) and (3.6) we get:

$$\dot{\tilde{P}}_{i1} = \dot{P}_{i1} - \dot{P}_{i1@Equi}$$
$$\dot{\tilde{P}}_{i1} = c_1\tilde{m}_{i1} - c_2\tilde{x}_i$$
$$\dot{\tilde{P}}_{i2} = c_3\tilde{m}_{i2} + c_4\tilde{x}_i$$

where c_1,c_2,c_3 and c_4 are given in the appendix.

3.2.2 Linearized Valve Dynamic Equations

The linearized equation relating mass flow rate out of the valves to the spool position is given below:

$$\dot{\tilde{m}}_{v1} = c_9\tilde{x}_{v1}$$
$$\dot{\tilde{m}}_{v2} = c_{10}\tilde{x}_{v2}$$

where c_9 and c_{10} are given in the appendix.

3.2.3 Linearized Tube Modeling Equations

The linearized equations of the tube models are given in the below equations:

$$\dot{\tilde{m}}_{L1} = \frac{A}{L}\tilde{P}_{m1} - \frac{A}{L}\tilde{P}_{L1} - \frac{32\mu}{\rho D^2}\tilde{m}_{L1}$$
$$\dot{\tilde{m}}_{L2} = \frac{A}{L}\tilde{P}_{m2} - \frac{A}{L}\tilde{P}_{L2} - \frac{32\mu}{\rho D^2}\tilde{m}_{L2}$$

3.3 Linearized Model in State space form

The model equations can be simplified and represented in state space format, the state vector X is given by: $X = [x_m; \dot{x}_e; P_s; \dot{m}; x_m; \dot{x}_m; P_m]$. The states equations are:

$$\dot{x}_e = \dot{x}_e \tag{3.13}$$

$$\ddot{x}_e = \frac{-1000}{m_p k_e} x_e - \frac{1000}{m_p(\beta + B_e)} \dot{x}_e - \frac{1000}{0.1 m_p A_p} P_s \tag{3.14}$$

$$\dot{P}_s = (c_6 + c_8)\dot{x}_e + (c_7 + c_5)\dot{m} \tag{3.15}$$

$$\ddot{m} = -c_{11} P_s - c_{22} \dot{m} + c_{11} P_m \tag{3.16}$$

$$\dot{x}_m = \dot{x}_m \tag{3.17}$$

$$\ddot{x}_m = \frac{-1000}{m_p} x_m - \frac{1000}{m_p \beta} \dot{x}_m + \frac{1000}{0.1 m_p A_p} P_m + \frac{1000}{m_p} F_h \tag{3.18}$$

$$\tag{3.19}$$

$$\dot{P}_m = \frac{-c_{12}}{(c_1 + c_{12})(c_1 + c_3)} \dot{m} - \frac{c_{12}}{(c_1 + c_{12})(c_2 + c_4)} \dot{x}_m -$$

$$= \frac{K_v c_{12}}{(c_1 + c_{12})(c_1 c_9 + c_3 c_{10})} P_m + \frac{K_v c_{12}}{(c_1 + c_{12})(c_1 c_9 + c_3 c_{10})} u$$

Where $c_1, c_2, c_3, c_4, c_5, c_6, c_7, c_8, c_9, c_{10}, c_{11}, c_{12}$ and c_{22} are constants defined in the appendix, the numbers included in this state space form (1000 and 0.1) are due to unit convergence, the used units are mentioned in appendix B. The output equation is:

$$y = x_m - x_s \tag{3.20}$$

The system is 7th order, the transfer function having input as valve position and output position difference between master and slave actuators is given by equation (3.22):

$$T(s) = \frac{Y(s)}{X_v(s)} = C(sI - A)^{-1} B + D \tag{3.21}$$

$$T(s) = \frac{-5.32 \cdot 10^5 s^4 - 1.08 \cdot 10^9 s^3 - 3.89 \cdot 10^{10} s^2 - 3.95 \cdot 10^{12} s - 7.38 \cdot 10^{11}}{s^7 + 2085 s^6 + 1.66 \cdot 10^5 s^5 + 1.92 \cdot 10^7 s^4 + 6.77 \cdot 10^8 s^3 + 1.92 \cdot 10^{10} s^2 + 3.57 \cdot 10^9 s} \text{mm} \tag{3.22}$$

The system can be further reduced to a second order system. Using the matlab command "reduce", the transfer function obtained is given by equation (3.23):

$$T(s)_{reduced} = \frac{35.58 s - 7245}{s^2 + 35.03 s} \tag{3.23}$$

The bode plot of both original and reduced systems are shown in figure (3.7).

13
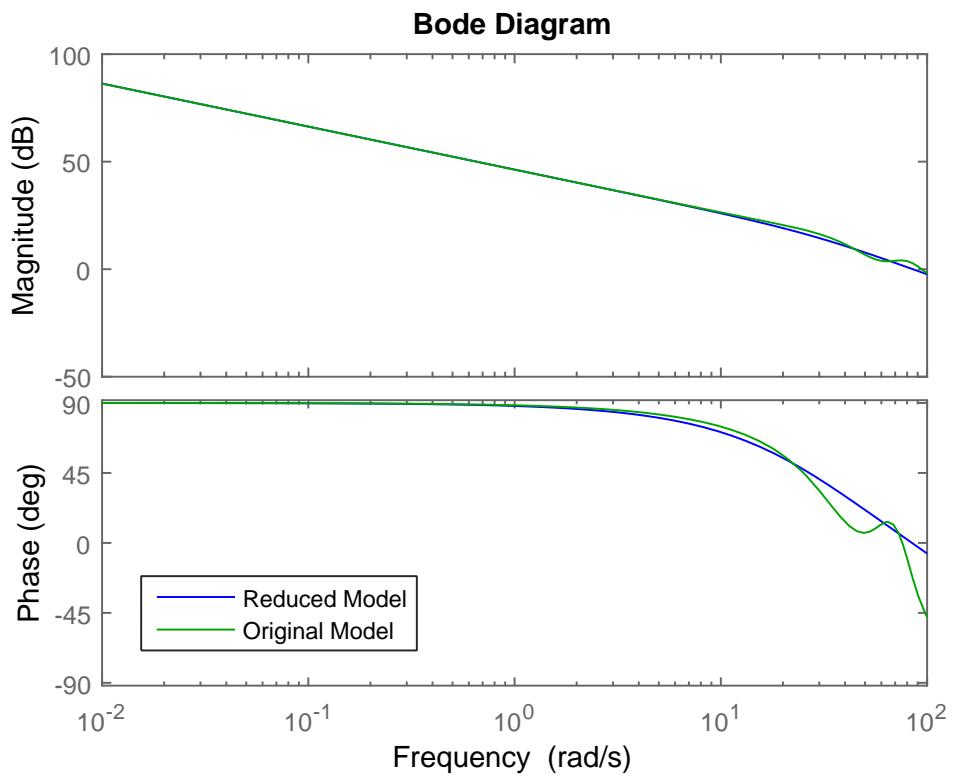
Figure 3.7: Open loop frequency response comparison

Chapter 4

System Analysis

4.1 Transparency Assessment

Transparency assessment is done by comparing the impedance of the teleoperator Z_t, which is the impedance transmitted to the human operator, to the impedance of the environment Z_e as shown in Figure (1.2). The impedance of the teleoperator Z_t is given by equation (1.3), and the environment impedance Z_e is given by equation (1.4). The environment can be modeled as a simple spring-damper system as shown in Figure (4.1), the environment impedance in this case is given by equation (4.1).

$$Z_e = \frac{B_e s + K_e}{s} \qquad (4.1)$$
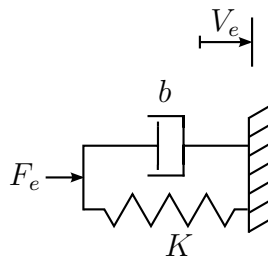
Figure 4.1: Environment representation

Ideally, the transparency ratio should be unity. In other words, the impedance transmitted to the human operator should be made equal to the impedance of the environment, so the human operator feels exactly the environment impedance, see figure (1.2). Linearizing nonlinear model equations is helpful in assessing how design parameters, such as cylinder or tube diameters and lengths, affect transparency and stability margin. The impedance is frequency dependent, thus the transparency ratio can also be represented in a bode plot. The aim of a control design is to get a transparency ratio of

0 dB for low operating frequencies, and have a high cutoff frequency while maintaining stability.

Proportional position control with cascaded pressure feedback was applied to the system in [6], position difference of the master and slave cylinders is fed back to the controller that controls the valve spool positions as shown in figure (4.2). This controller yielded good results regarding transparency while maintaining stability for a low stiffness environment. The control parameters that ensure tracking of master and slave with guaranteed stability were found to be: $K_p = 2.9\text{V/bar}$ and $K_s = 2.4\text{N/mm}$.
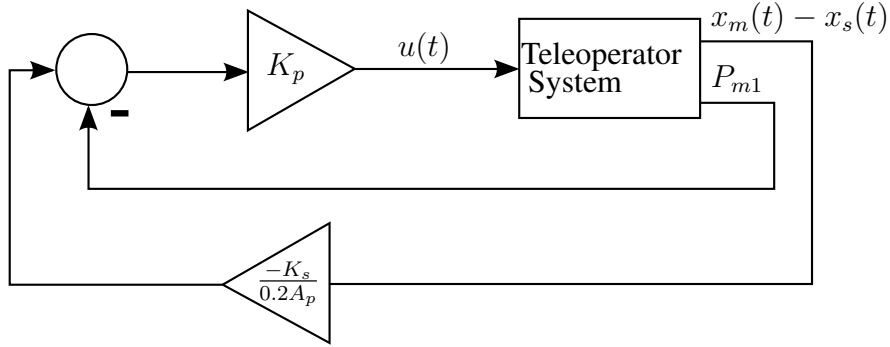
Figure 4.2: Proportional Controller

The teleoperator's impedance Z_t is tested when the teleoperator is facing a soft environment modeled as a simple spring and damper system as shown in Figure (4.1), with spring stiffness $K_e = 0.1 \text{ N/mm}$ and damping $B_e = 0.5 \text{ N.s/mm}$ and using the same control parameters and dimensions as in [6]. In Laplace domain, the environment impedance is written as:

$$Z_e = \frac{0.5s + 0.1}{s} \frac{N.s}{mm} \tag{4.2}$$

The bode plots of Z_t and Z_e, given by equations (1.3) and (1.4), are shown in figure (4.3). It can be seen that the magnitudes of Z_t and Z_e are dicreasing with a rate of -20 dB/decade for frequencies less than $\frac{K_e}{B_e} = 0.2 \text{ rad/s}$, where the environment behaves like a pure spring, for frequencies above of 0.2 rad/s, the environment behaves like a pure damper. For frequencies higher than 5 rad/s, the magnitudes are starting to move far away from each other, and the phase difference is between $30°$ and $130°$ which means that the impedance of the environment is not directly fed to the human operator by the teleoperator, and the system will become less transparent. Bode plot of the transparency ratio $\frac{Z_t}{Z_e}$ is shown in Figure (4.4): The ideal 0 dB transparency ratio magnitude is maintained at very low frequencies till 5 rad/s, phase shift of 0 deg is maintained till 0.5 rad/s. At higher frequencies, the teleoperator starts loosing its transparency, magnitude of Z_t/Z_e is moving away from 0 dB and phase lag is moving away from 0 deg thus the human operator will not be able to feel the true environment impedance that is transmitted with time delay too. To compare the transparency result of our system with the "transparency optimized architecture" done by Lawrence
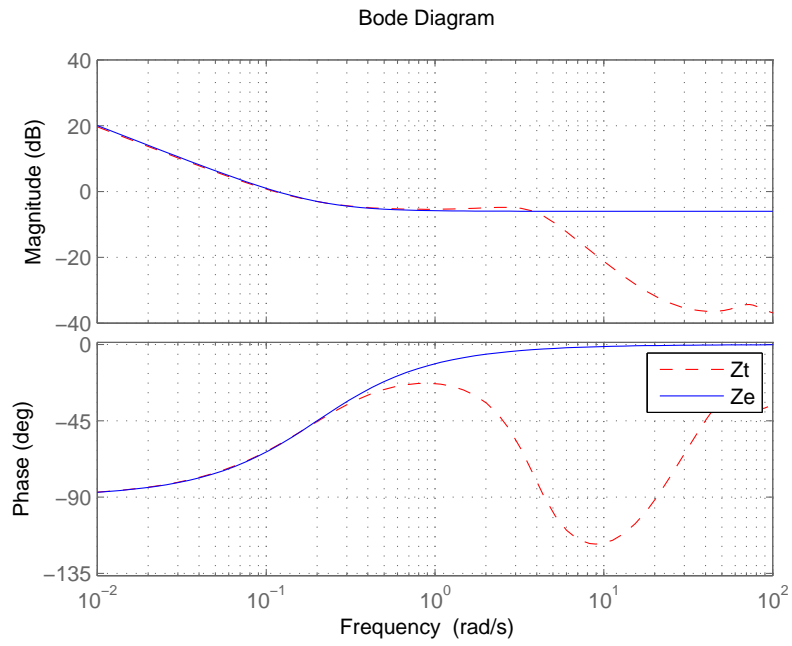
Figure 4.3: Bode Plot of the teleoperator impedance Z_t and environment impedance Z_e
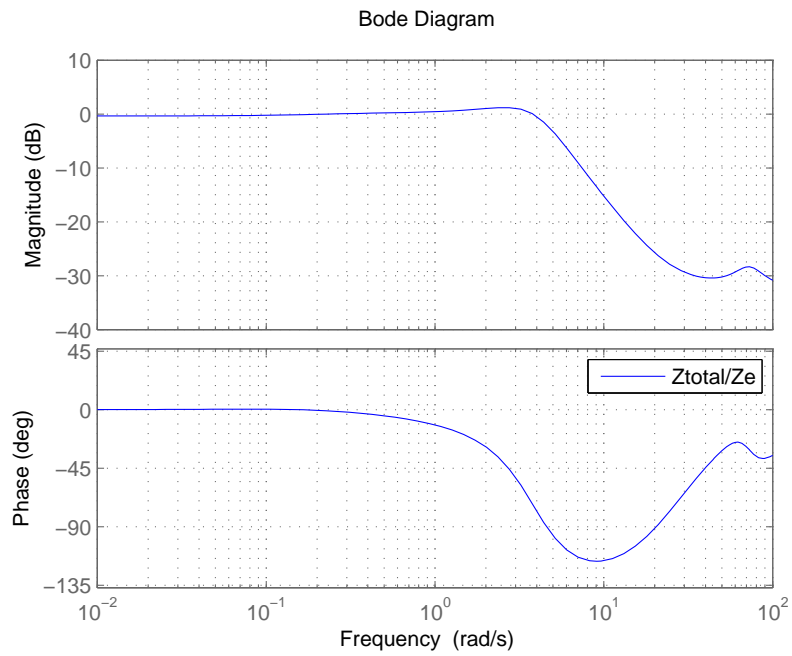
Figure 4.4: Bode Plot of transparency ratio of the system

in [5], the system is tested with the environment impedance $Z_e = \frac{17.51}{s}$ (modeling the environment as a spring with $K_e = 17.51$ N/mm), as done in [5], the results are shown in figure (4.5). For low frequencies, i.e. less than 1 rad/s, lawrence system presented
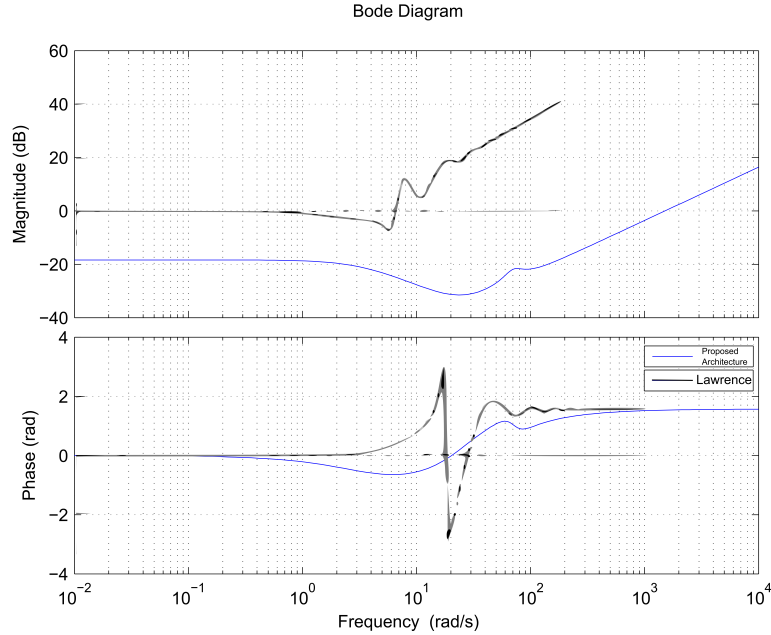
Figure 4.5: Bode Plot of transparency ratio of proposed system against Lawrence result

good transparency where the transparency ratio magnitude is 0 dB, and the phase is also $0°$. When frequency increases, the transparency ratio starts to move far from the ideal case. The proposed system presented less satisfactory transparency results, even at very low operating frequencies, magnitudes of Z_t and Z_e are different, and with frequency increase, both magnitude and phase shift are different for these impedances. This is due to the high stiffness environment facing the slave actuator, the previously used proportional controller gains aren't able to maintain same performance of the controller. Lawrence system is more transparent than the proposed architecture, and his results were obtained after improving the architecture. So, as a conclusion, improving architecture and communication links can improve the transparency ratio.

4.2 Sensitivity Study

This section helps to understand the effect of physical and control parameters in system behavior, and how it affects the transparency ratio. Starting by modification of the tube diameter, the original tube diameter is $D_t = 4$mm.
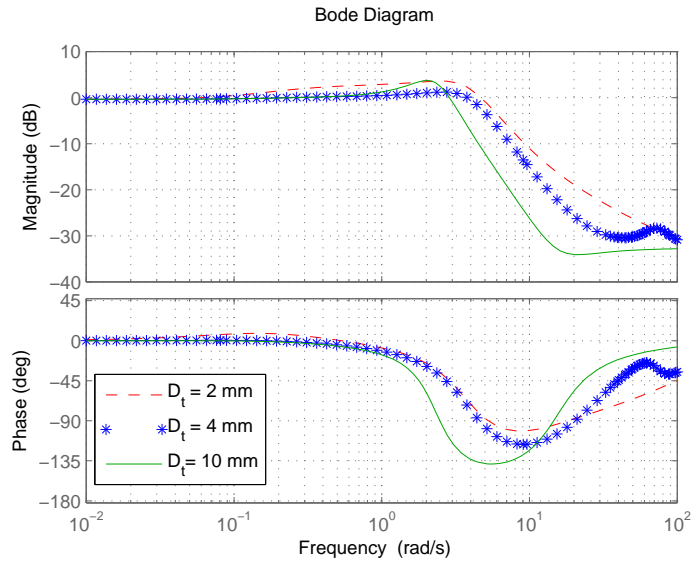
Figure 4.6: Bode Plot of transparency ratio of the system for different tube diameters

Figure (4.6) shows that dicreasing tube diameter leads for the impression that the environment is much more damped than it actually is. While increasing tube diameter leads to the impression that system is less damped and the large phase lag leads to impression that system is springy, not viscous damping. Changing the pneumatic lines length, the original length is $L_t = 5m$.
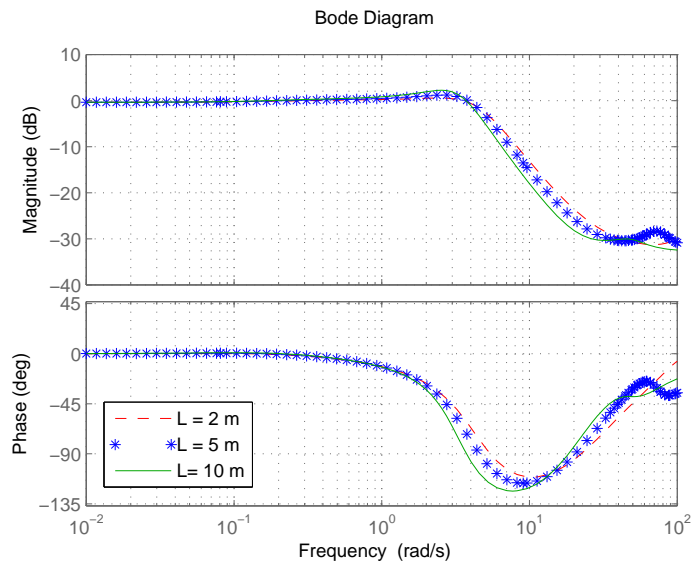
Figure 4.7: Bode Plot of transparency ratio of the system for different tube length

Regarding the tube length change, results are shown in figure (4.7), it is noticed

that dicreasing tube length leads to better system transparency at high frequencies, while increasing it is not capable of improving it. Thus change in both tube diameter or length can affect system's performance because it has direct influence on mass flow rate and friction facing the flow of air inside the tubes.

Changing the control parameter K_p and K_s, the original control parameters were $K_s = 2.4$ and $K_p = 2.9$, results are shown in figure (4.8).
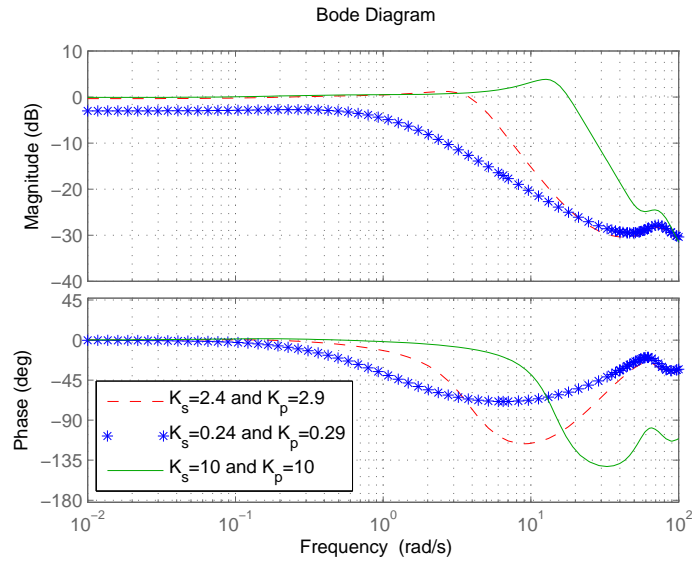
Figure 4.8: Bode Plot of transparency ratio of the system for different control parameters

Dicreasing controller gains K_s and K_p causes loose of transparency at all operating frequencies compared to original gains, while increasing it causes the transparency ratio magnitude and phase shift to be maintained as zero till higher frequency, but this does not mean that the system is more transparent because stability is lost in this case. To conclude this section, we can say that geometry parameters such as tube length and diameter, and control parameters have direct influence on the transparency ratio, so one way to improve system's behavior is by modifying the geometry, or by designing a better controller.

Chapter 5

Linear Control Design

5.1 Lead Compensator Design Process

Using a lead compensator can increase the bandwidth of a system without loss of phase margin [16]. Therefore, a lead compensator with cascaded pressure feedback is designed to improve the system performance, i.e. to control the slave piston to follow the master piston and supply the required force feedback to the human operator as shown in figure (5.1). It is desired to maintain a phase margin of $\gamma \approx 50°$ at a gain cross-over frequency of $\omega_{gc} = 50 \, \text{rad/s}$ so that the bandwidth of the system increases. The following compensator transfer function is used:

$$T(s) = 5\frac{0.052s + 1}{0.0076s + 1} \tag{5.1}$$

The open loop frequency response that reveals the stability margin is plotted in Figure (5.2) for both, the plant with proportional control and with lead compensator. The environment is modeled as a simple spring and damper system as shown in Figure (4.1), with spring stiffness $K_e = 0.1 \, \text{N/mm}$ and damping $B_e = 0.5 \, \text{N.s/mm}$.

In Laplace domain, the environment impedance is written as:

$$Z_e = \frac{0.5s + 0.1}{s} \, \frac{N.s}{mm} \tag{5.2}$$
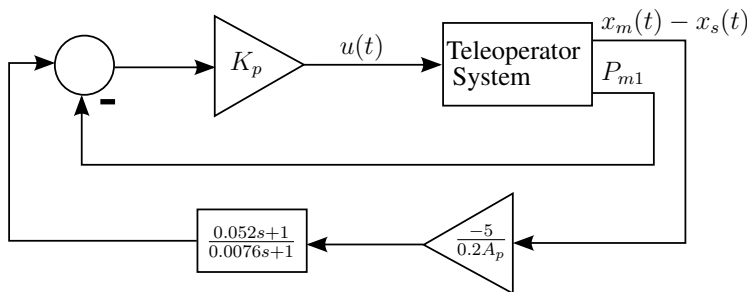
Figure 5.1: Lead Compensator Controller

Referring to Figure (3.1), the input of the open loop frequency response is the valve input u and the output is the error signal $x_m - x_s$.
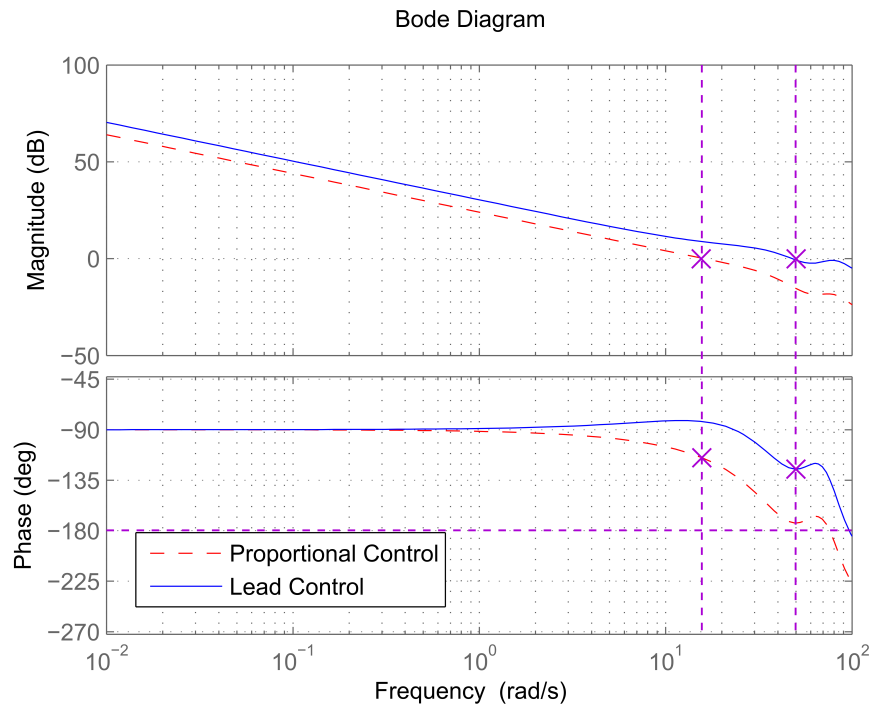
Figure 5.2: Open loop frequency response comparison between plant with proportional position control and lead compensator, input is dimensionless valve input signal u ($u = 1$ is valve fully opened), output is position error between master and slave cylinders

One can see how with the lead compensator the new gain crossover frequency is shifted to the right, $\omega_{\mathrm{gc}} = 50\,\mathrm{rad/s}$, and the phase margin is maintained. Therefore, for the transparency ratio $\frac{Z_t}{Z_e}$, we may expect a higher bandwidth for the lead compensated system. Figure (5.3) shows the transparency ratio of the system with the two different linear control laws.
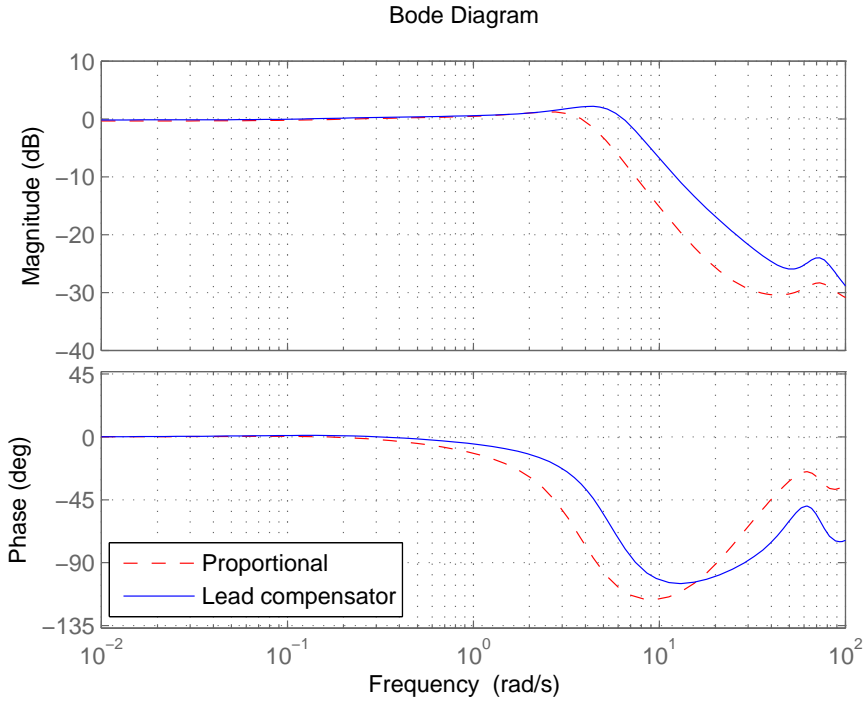
Figure 5.3: Bode plot of transparency ratio for system with proportional position feedback and system with lead compensator feedback, input is the velocity of the human operator hand and output is the force reflected to the operator

The ideal $0\,\mathrm{dB}$ transparency ratio magnitude is achieved at low frequencies, with a phase of $0°$ for both controllers. At higher frequencies, the teleoperator starts losing transparency as the magnitude of Z_t/Z_e moves away from 0 dB. It is seen that the lead compensator control improves transparency for higher frequencies.

To illustrate the fact that a change in the environment parameters directly affect the transparency, Figure (5.4) compares the transparency achieved with the lead compensator for the original and a new environment 5 times more stiff and damped, the new environment impedance is given by equation (5.3).

$$Z_e = \frac{2.5s + 0.5}{s} \ \frac{N.s}{mm} \tag{5.3}$$

23
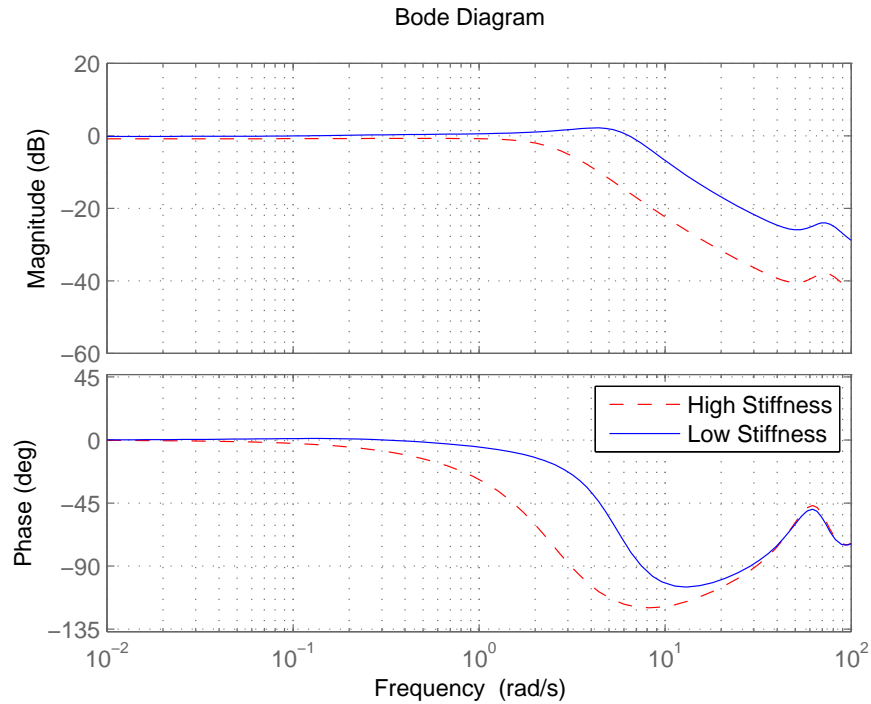
Figure 5.4: Bode Plot of transparency ratio for different environments for lead compensator

It can be seen that the lead compensator does not maintain the same level of transparency. As the remote environment gets stiffer, the relatively low stiffness of the teleoperator becomes more apparent. This is expressed by the fact that the transparency magnitude and phase is dropping from the $0\,\mathrm{dB}$ and $0\,^\circ$ line starting at lower frequencies.

5.2 Linear Control Simulation Results

To visualize the output of the system, a pulse force input to the master (Amplitude = 5 N, Period = 5s, Pulse width= 50 %) is applied, and the teleoperator's response while acting against environment impedance $Z_e = \frac{0.5s+0.1}{s}$ is visualized. Figure (5.5) shows the force acting against the slave actuator versus the force transferred to the human operator, and figure (5.6) shows the positions of master and slave actuators for both proportional controller and lead compensator.
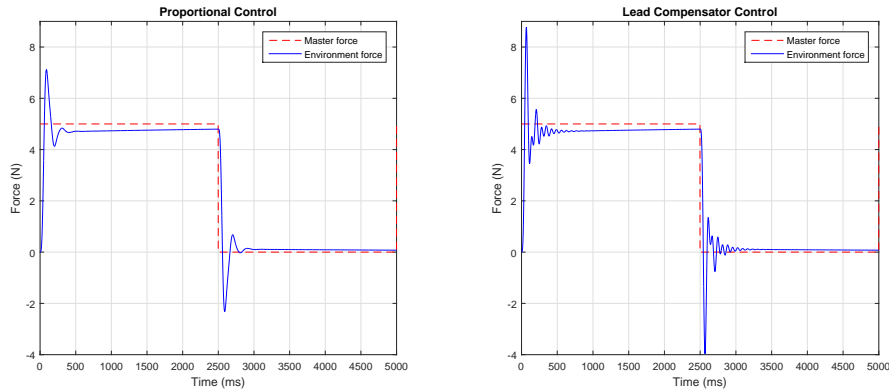
Figure 5.5: Forces comparison
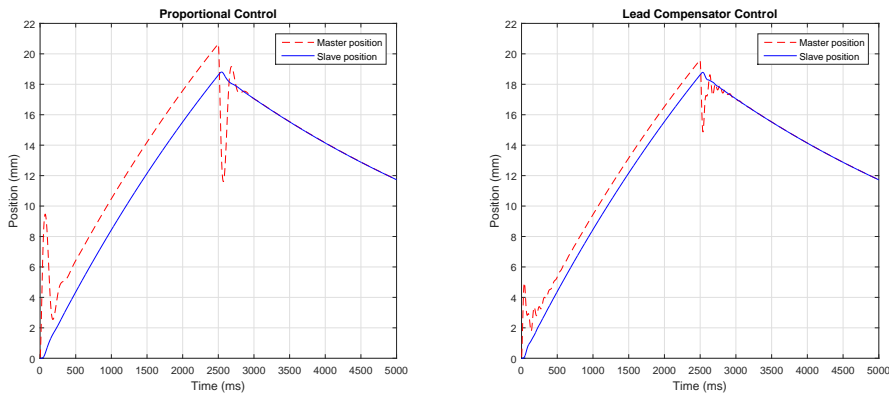
Figure 5.6: Positions comparison

Proportional controller and lead compensator presented acceptable performance regarding transparency and stability for low operating frequencies and for certain operating environment impedances. Once environment impedance changes, or human operator exerts an unexpected movement, the system transparency is directly affected. These results implies that the proposed linear controllers are not capable to provide expected performance if impedance of human arm or environment impedance change during the operation. A nonlinear controller that can adapt to these changes and can improve system performance is designed in the next chapter.

Chapter 6

Adaptive Control Design

The control purpose can be described as a tracking problem. The purpose is to make the slave piston position x_s to track the master piston position x_m and thus an indirect self-tuning regulator (STR) is chosen to address this problem. The system is non-minimum phase, it has zeros outside the unit circle in discrete-time representation, and thus the indirect self-tuning regulator is designed without zero cancellation.

This control paradigm uses a recursive least squares (RLS) algorithm to estimate the plant parameters [17]. The controller parameters are in turn updated based on the estimation of the system parameters. A block diagram of the adaptive controller is shown in Figure (6.1).
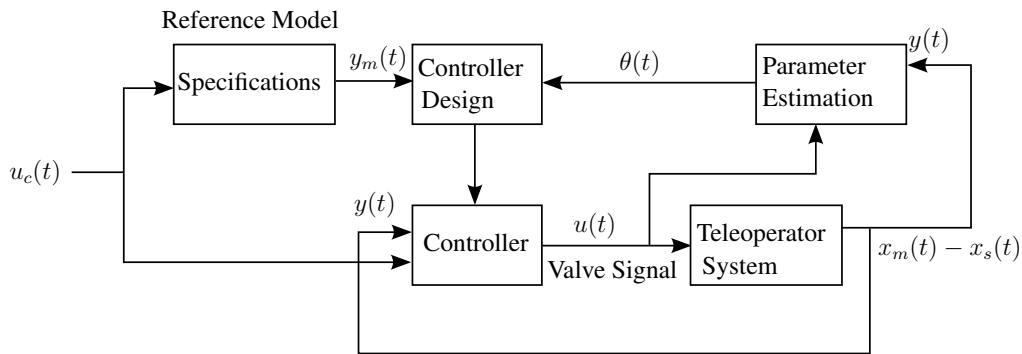
Figure 6.1: Adaptive control system

The adaptive controller is designed so that the system output $x_m(t) - x_s(t)$, the position error between the master and slave actuator, tracks the reference input $u_c(t)$, which is in our case zero. The parameter estimation block estimates the system parameters based on the system output $x_m(t) - x_s(t)$ and the control input, the valve signal $u(t)$. The "Controller Design" block supplies the "Controller" block with updated parameters to compute the control signal $u(t)$, based on the estimated system parameters, and on the desired model output. The "Controller" block generates the actual system input, the valve input signal u, based on the system output $x_m(t) - x_s(t)$

and the desired system output (the reference input) $u_c(t)$.

6.1   Parameter Estimation

The teleoperator transfer function in discretized form $G(z)$ with the input and output defined as stated above, is given by:

$$G(z) = \frac{B(z)}{A(z)} = \frac{b_0 z^5 + b_1 z^4 + b_2 z^3 + b_3 z^2 + b_4 z + b_5}{a_0 z^6 + a_1 z^5 + a_2 z^4 + a_3 z^3 + a_4 z^2 + a_5 z + a_6} \qquad (6.1)$$

Dividing both levels by z^6, we get:

$$A(z^{-1})y(t) = B(z^{-1})u(t) \qquad (6.2)$$

$$(a_0 + a_1 z^{-1} + ... + a_6 z^{-6})y(t) = (b_0 z^{-1} + b_1 z^{-2} + ... + b_5 z^{-6})u(t) \qquad (6.3)$$

The system expressed as a difference equation can be written as:

$$y(t) = -a_1 y(t-1) - ... - a_6 y(t-6) + b_0 u(t-1) + ... + b_5 u(t-6) \qquad (6.4)$$

Thus, the parameter vector $\theta(t)$, and the regression vector $\varphi^T(t)$ are written as:

$$\theta(t) = [a_1, ..., a_6, b_0, b_1, ..., b_5]^T$$
$$\varphi^T(t) = [-y(t-1), -y(t-2), ..., -y(t-6), u(t-1), u(t-2), ..., u(t-6)]$$

And thus the output $y(t)$ is written as:

$$y(t) = \varphi^T(t)\theta \qquad (6.5)$$

Recursive least square estimation is given by [17]:

$$\hat{\theta}(t) = \hat{\theta}(t-1) + K(t)(y(t) - \varphi^T(t)\hat{\theta}(t-1))$$
$$K(t) = P(t)\varphi(t) = P(t-1)\varphi(t)(\lambda I + \varphi^T(t)P(t-1)\varphi(t))^{-1}$$
$$P(t) = (I - K(t)\varphi^T(t))P(t-1)/\lambda$$

where $P(t) = (\varphi^T(t)\varphi(t))^{-1}$, $K(t)$ is a vector of weighting factors that tell how the correction and the previous estimate should be combined, and λ is a forgetting factor that introduces time-varying weighting of data such that $0 < \lambda \leq 1$. The parameters $\theta(t)$ are initialized with reasonable values that can represent the nominal system, and the *P(t)* matrix is initialized with a 12x12 identity matrix multiplied by a large number to achieve asymptotic output tracking. Parameter estimation can be done using the projection algorithm too which is more computationally efficient than RLS used in this context. The sampling time of the parameter estimation is chosen as 20 ms while the controller sampling time is 1 ms, system parameters are not supposed to be changing very fast (as the controller sampling rate) that's why it is not necessary to estimate

parameters at each sampling time of the controller, this choice is more computationally efficient. The parameter vector $\theta(t)$ is initialized with the approximate parameters of the system operating with no physical environment is facing the slave actuator, the P matrix is initialized with an identity matrix multiplied by 100, which results in fast convergence. The forgetting factor is chosen as $\lambda = 1$ after performing several tests, so it is neglected, and the plant parameters are converging fastly to its correct values with this chosen λ.

6.2 Controller Design

A control law that yields two degrees-of-freedom, feedforward and negative feedback, is given by:

$$Ru(t) = Tu_c(t) - Sy(t) \tag{6.6}$$

Where R,T and S are polynomials determined by the "Controller Design" block based on the estimation of plant parameters and on the reference model. The desired performance specification are stipulated by the reference model which is given the following equation:

$$\frac{B_m(s)}{A_m(s)} = \frac{\omega_n^2}{s^2 + 2\zeta\omega_n s + \omega_n^n} \frac{\psi^4}{(s+\psi)^4} \tag{6.7}$$

where ω_n is the natural frequency of the second order polynomial, ζ is the damping ratio and ψ is parameterized as a non-dominant pole far left from the second order model poles; these poles are necessary to increase the order of the model to 6th order to respect the causality conditions: deg $A_m(z) =$ deg $A(z) = 6$ and deg $B_m(z) =$ deg $B(z) = 5$. The desired response is achieved by setting the characteristic natural frequency $\omega = 6\pi \, \mathrm{rad/s}$, damping ratio to be unity and all other poles of the reference model to a very high value ($\psi = 10^5 \, \mathrm{rad/s}$). The discretized transfer function of the reference model is given by:

$$\frac{B_m(z)}{A_m(z)} = \frac{b_{m0}z^5 + b_{m1}z^4 + b_{m2}z^3 + b_{m3}z^2 + b_{m4}z + b_{m5}}{z^6 + a_{m1}z^5 + a_{m2}z^4 + a_{m3}z^3 + a_{m4}z^2 + a_{m5}z + a_{m6}} \tag{6.8}$$

The indirect self-tuner is designed without zero cancellation, thus the polynomial B(z) can be written as:

$$B(z) = B^+(z)B^-(z)$$
$$B^+(z) = 1$$
$$B^-(z) = B(z)$$

28

The causality conditions that specify the relative degrees of the observer polynomial A_0, R, S and T are:

$$deg A_o = deg A - deg B^+ - 1 = 5$$
$$deg R = deg(A_0 A_m) - deg A$$
$$des S \leq deg R$$
$$deg T \leq deg R$$

The system model is given by: $Ay(t) = Bu(t)$. The control signal $u(t)$ which corresponds to the valve spool position, is obtained from eq (6.6) as:

$$u(t) = \frac{T}{R} u_c(t) - \frac{S}{R} y(t) \tag{6.9}$$

Elimination of u between the system model and the control law, we get the system output $y(t)$ as a function of the commanded input, $u_c(t)$:

$$y(t) = \frac{BT}{AR + BS} u_c(t) \tag{6.10}$$

The pole placement design is done with diophantine equation:

$$AR + BS = A_0 A_m \tag{6.11}$$

Where polynomials R and S are computed. Based on the causality conditions, R and T are fifth order polynomials and S is a second order polynomial:

$$R(z) = r_0 z^5 + r_1 z^4 + r_2 z^3 + r_3 z^2 + r_4 z + r_5$$
$$S(z) = s_0 z^2 + s_1 z^1 + s_2$$

The observer polynomial $A_0(z)$ is of 5th order, in discrete form it can be written as:
$$A_0(z) = (z + O0)(z + O1)^4 \tag{6.12}$$

which can be expanded in the form:

$$A_0(z) = z^5 + a01 z^4 + a02 z^3 + a03 z^2 + a04 z + a05 \tag{6.13}$$

In discrete time analysis, using small values for observer poles leads to a fast observer, while increasing the value leads to slower observer [18]. Based on the required performance, and using trial and error, the observer polynomial parameters are specified as: $O0 = 0.3$ and $O1 = 0.32$.

From equation (6.10), we have:

$$\frac{y(t)}{u_c(t)} = \frac{BT}{AR + BS} = \frac{B_m}{A_m} \tag{6.14}$$

29

And thus, polynomial T is computed using:

$$T = \frac{A_m(1)}{B(1)}A_0 \tag{6.15}$$

In discrete form, $T(z)$ is written as:

$$T(z) = t_0 z^5 + t_1 z^4 + t_2 z^3 + t_3 z^2 + t_4 z + t_5 \tag{6.16}$$

The control signal $u(t)$ is saturated between -1 and 1 because it corresponds to the valve spool position, thus a maximum $u(t) = 1$ corresponds to full opening of the valve, or 100%. The control signal is then filtered with the filter having the following transfer function: $F(s) = \frac{1}{0.1s+1}$.

6.3 Adaptive Control Simulation Results and comparison with proportional control

This section presents simulation results of the proposed teleoperation system and controller operating in different conditions, changing both the physical environment in contact with the slave actuator and the human operator applied force.

To show the ability of the system to adapt to various environments, it is tested with different operating environments: human skin, fat, and muscle. The values of stiffness and damping of each environment were presented in [9] as:

1. Skin: K = $0.331\,\mathrm{N/mm}$ and B = $3 \cdot 10^{-6}\,\mathrm{N.s/mm^2}$

2. Fat: K = $0.083\,\mathrm{N/mm}$ and B = $10^{-6}\,\mathrm{N.s/mm^2}$

3. Muscle: K = $0.497\,\mathrm{N/mm}$ and B = $3 \cdot 10^{-6}\,\mathrm{N.s/mm^2}$

The three environments behave like a pure spring, damping is negligible. The three environment impedances are plotted in figure (6.2).
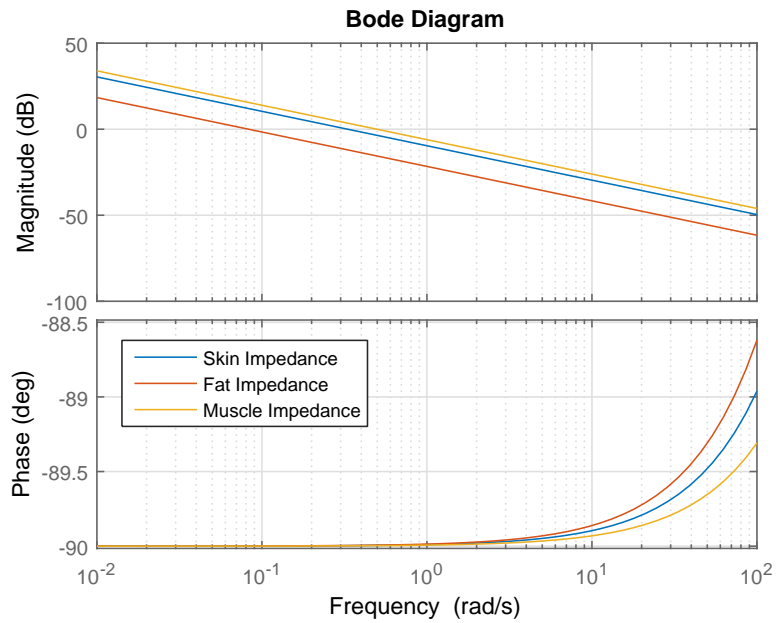
Figure 6.2: Skin, Fat and Muscle Impedances

6.3.1   Skin environment

The system is first tested against a human skin environment model, the actuator is free to move for the first 10 s, the applied force is $10\,\mathrm{N}$ at $0.5\,\mathrm{Hz}$ sinusoidal actuation. After 10 s it faces the human skin model. Results for master and slave positions are shown in figures (6.3) and (6.4) for adaptive and proportional controller respectively.

Figure 6.3: Master and slave pistons positions using the adaptive control and sinusoidal force input of 10 N. Actuator comes into contact with skin environment impedance after 10 s

Figure 6.4: Master and slave pistons positions using the proportional control and sinusoidal force input of 10 N. Actuator comes into contact with skin environment impedance after 12 s

The error between master and slave positions for both adaptive and proportional control is plotted in figure (6.5).

Figure 6.5: Error comparison between adaptive and proportional controllers. The applied force is 10 N, and actuator comes into contact with skin environment impedance after the free motion

In the beginning, the adaptive controller required around 3 s to adapt and presented smaller error than proportional control. After the change of environment, 6 s were needed to adapt and the error converged to around 2mm, while the error of the proportional controller increased to 20mm after the contact with the skin environment.

6.3.2 Fat environment

In the second test, the slave actuator is facing a human fat environment, the applied force is $10\,\mathrm{N}$ at $0.5\,\mathrm{Hz}$, the actuater is free to move for the first 10 s then it faces the human fat environment. Results for master and slave pistons positions for adaptive and proportional controllers are shown in figures (6.6) and (6.7) respectively.
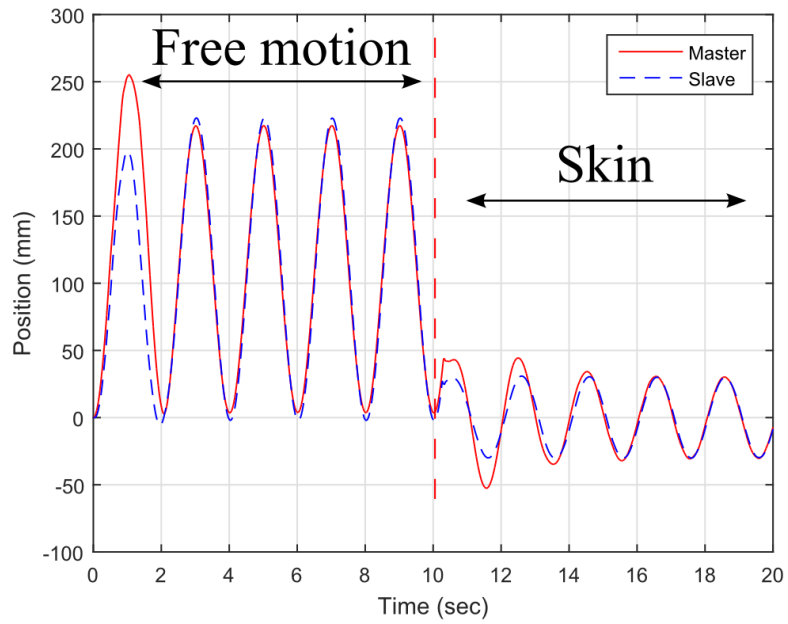
Figure 6.6: Master and slave pistons positions using the adaptive control and sinusoidal force input of 10 N. Actuator comes into contact with fat environment impedance after 10 s
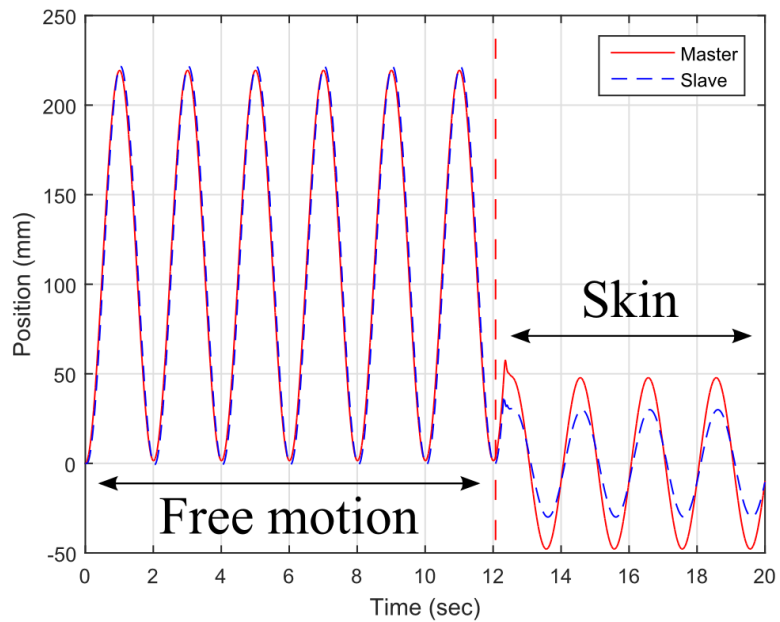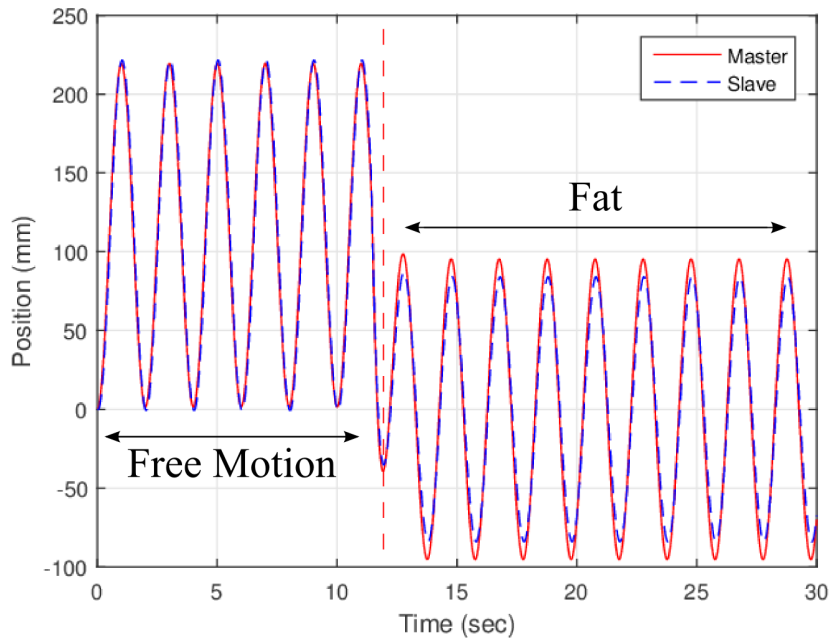
Figure 6.7: Master and slave pistons positions using the proportional control and sinusoidal force input of 10 N. Actuator comes into contact with fat environment impedance after 12 s

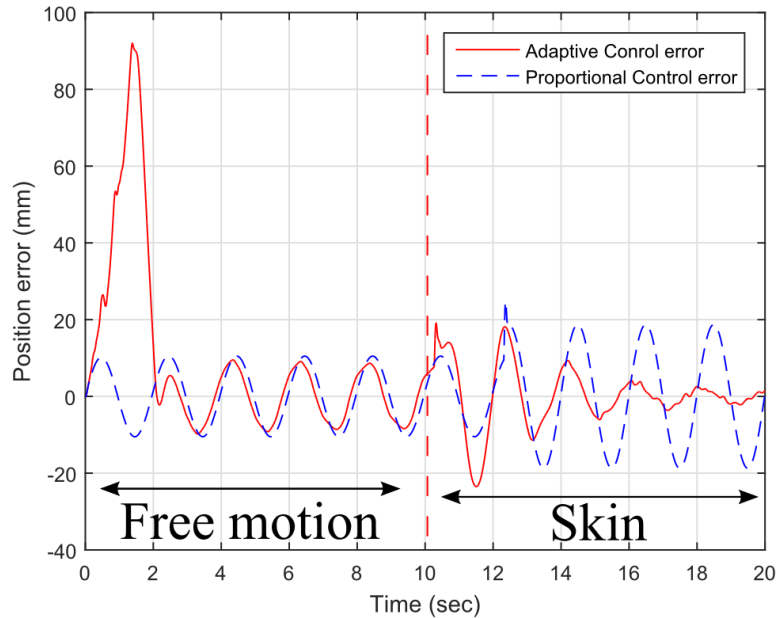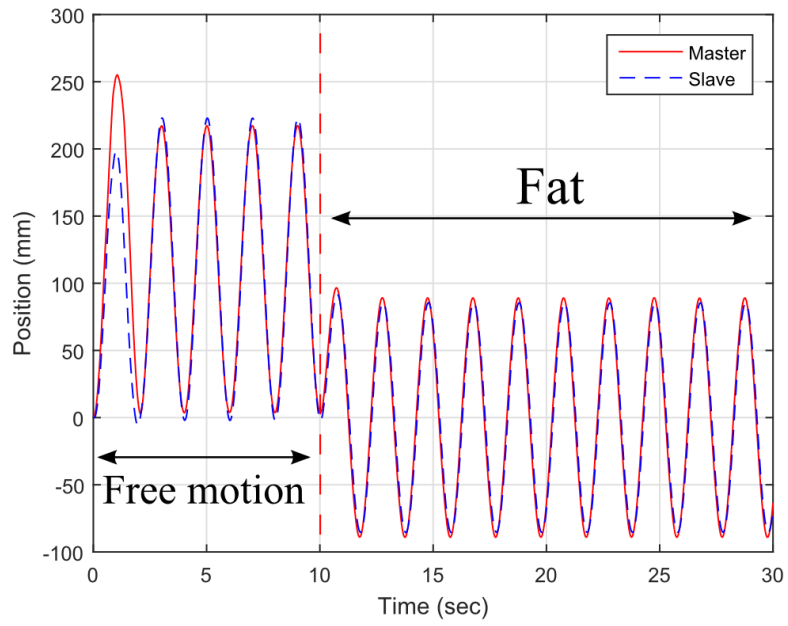The error between master and slave positions for both adaptive and proportional control is plotted in figure (6.8).

Figure 6.8: Error comparison between adaptive and proportional controllers. The applied force is 10 N, and actuator comes into contact with fat environment impedance after the free motion

As observed in the first test, the adaptive controller presented smaller error with and without the opposing environment, which is human fat in this case, and required around 3 to 4 s to adapt only with 10mm error. The proportional controller presented 14mm error after the contact with the fat environment.

6.3.3 Muscle Environment

Testing the system operating in muscle environment, changing the applied force each 10 s, starting with 10 N,1 N, 20 N and then removing the applied force for the last 10 s. Results for adaptive controller and proportional controller are shown in figures (6.9) and (6.10) respectively.
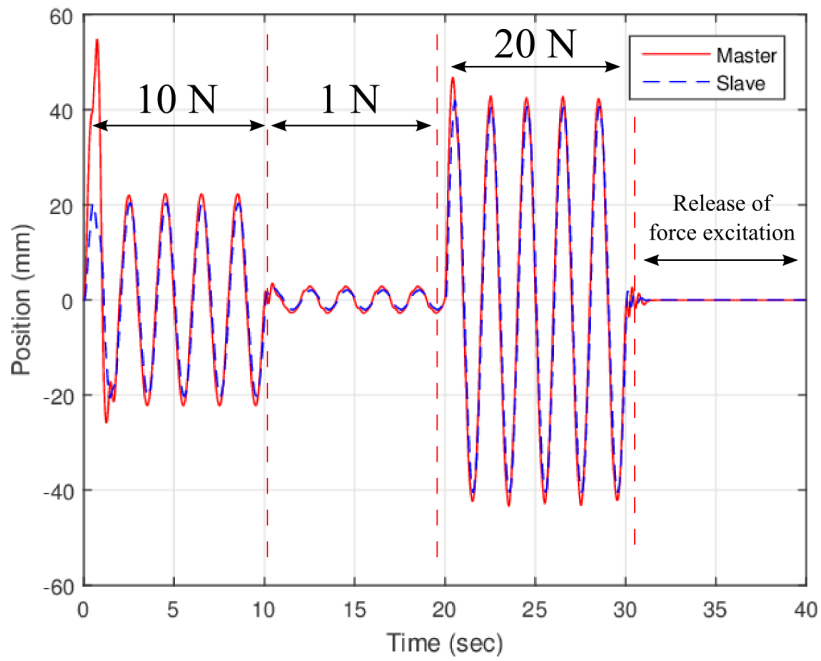
Figure 6.9: Master and slave pistons positions using the adaptive control and variable sinusoidal force input facing muscle environment
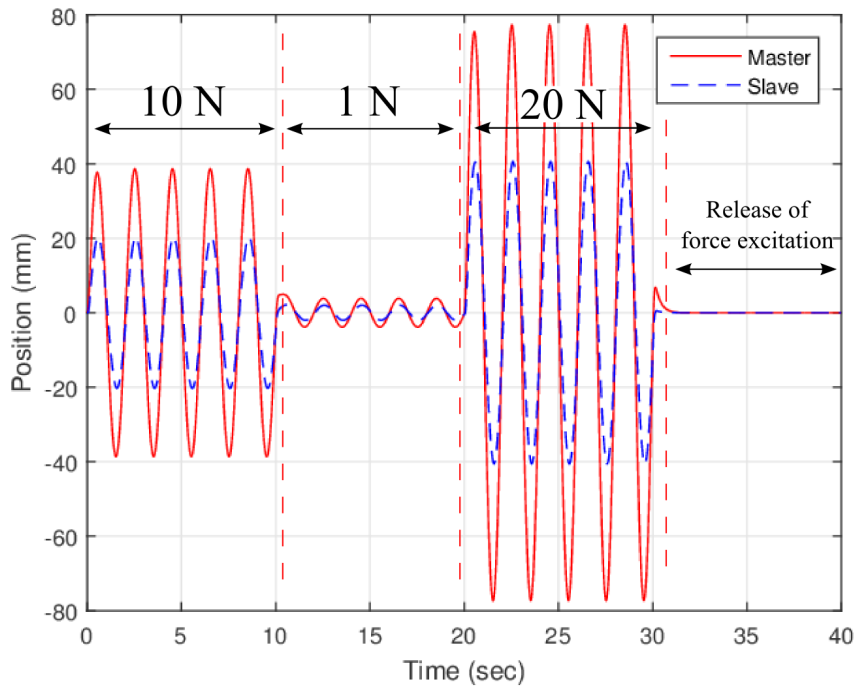
Figure 6.10: Master and slave pistons positions using the proportional control and variable sinusoidal force input facing muscle environment

37

The error between master and slave positions for both adaptive and proportional control is plotted in figure (6.11).

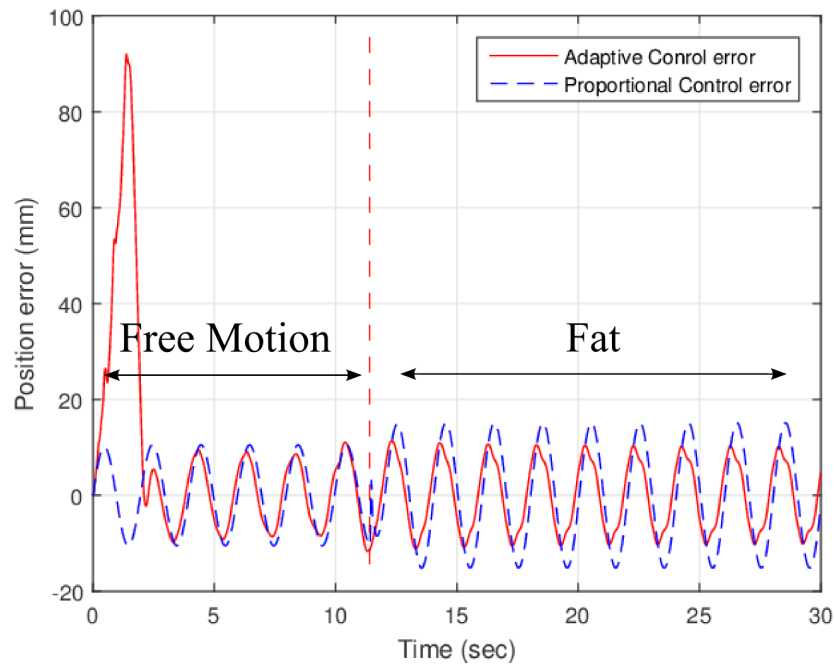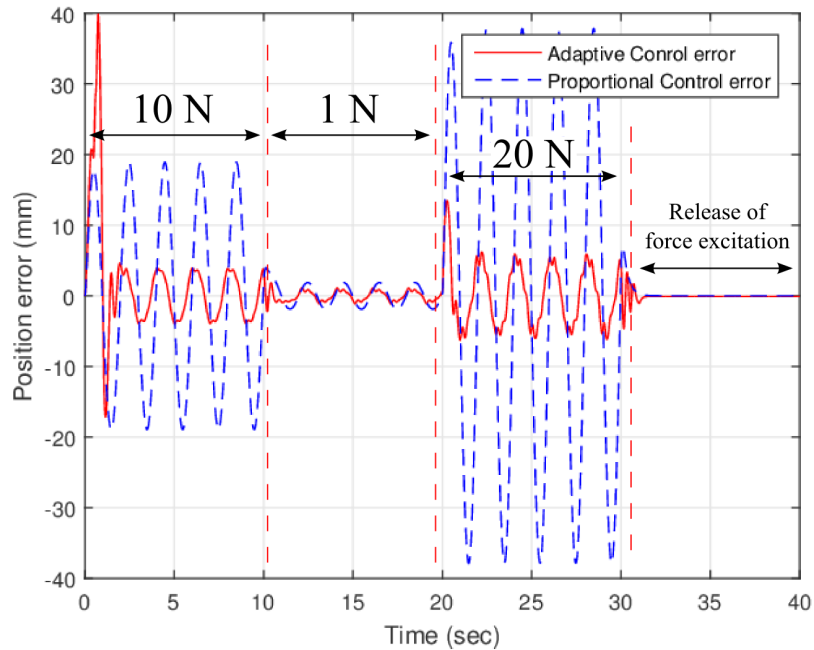Figure 6.11: Error comparison between adaptive and proportional controllers for variable sinusoidal force input facing muscle environment

In this test, first we can see the large error in the case of proportional controller due to the increased stiffness and damping of the environment, which is human muscle. The error increases with the increase of the applied force by the human operator. Adaptive controller is capable to adapt with this increase in environment stiffness, and with increase of the operator applied force with minimal error between master and slave pistons positions.

Chapter 7

Experimental Results

This chapter presents simulation and experimental results of the three controllers: proportional, lead compensator, and adaptive. Three physical environments were used to test the performance of each controller on the test rig: a stress ball, a sponge, and a stone. Stiffness and damping of the stress ball and the sponge were approximated by using the HOUNSFIELD H100KS materials testing machine as shown in figures (7.1 and 7.2).
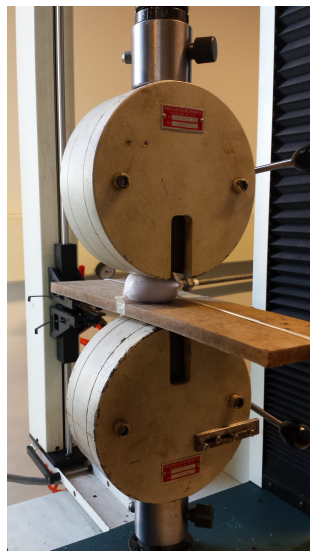
Figure 7.1: Testing the stress ball with HOUNSFIELD H100KS testing machine
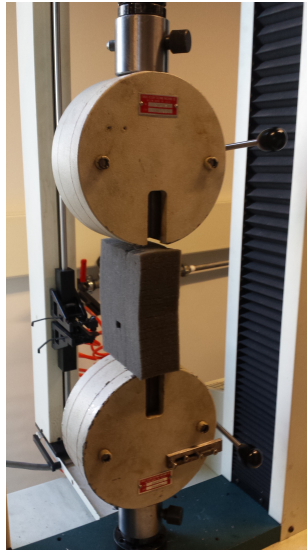
Figure 7.2: Testing the sponge with HOUNSFIELD H100KS testing machine

First, force is applied as steps, with constant time interval, force and displacement were collected as shown in figure (7.3).
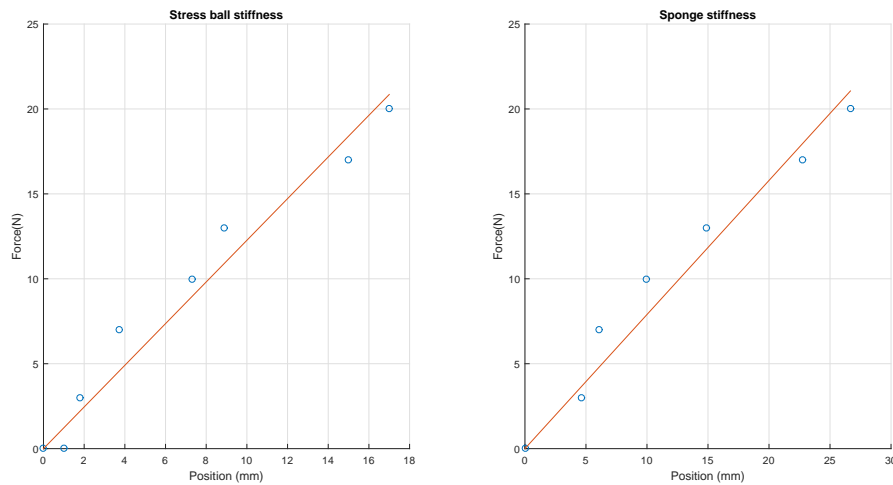
Figure 7.3: Stiffness force versus displacement for both stress ball and sponge

Force and displacement data are fitted with a straight line, the slope is the stiffness of of the environment K_e. Second, force is applied continuously, moving with a constant velocity through each environment, collecting the force at each time step. 3 velocities were used: $1.66\,\mathrm{mm/s}$, $2.5\,\mathrm{mm/s}$ and $3.33\,\mathrm{mm/s}$. The damping force is found by subtracting the stiffness force from the total force: $F_d = F_t - F_k$. The results for F_t and F_d for stress ball and sponge are shown in figures (7.4) and (7.5) respectively.
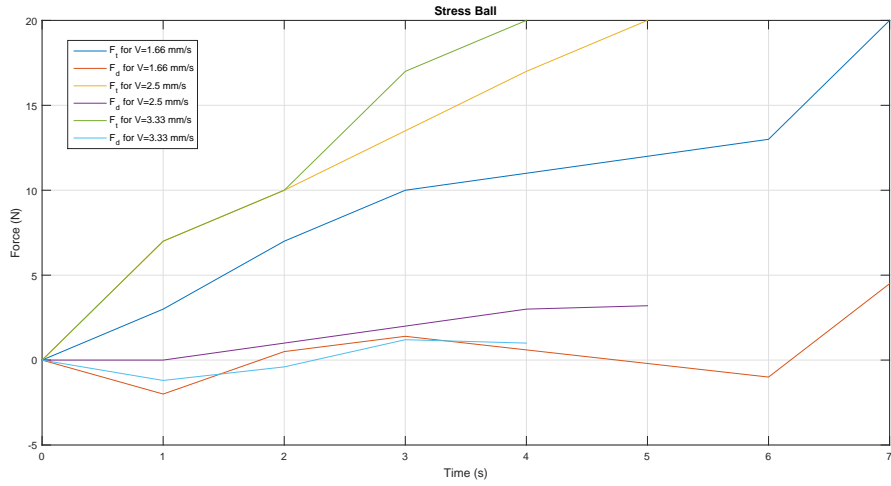
Figure 7.4: Total force F_t and damping force F_d for the 3 applied velocities, stress ball environment
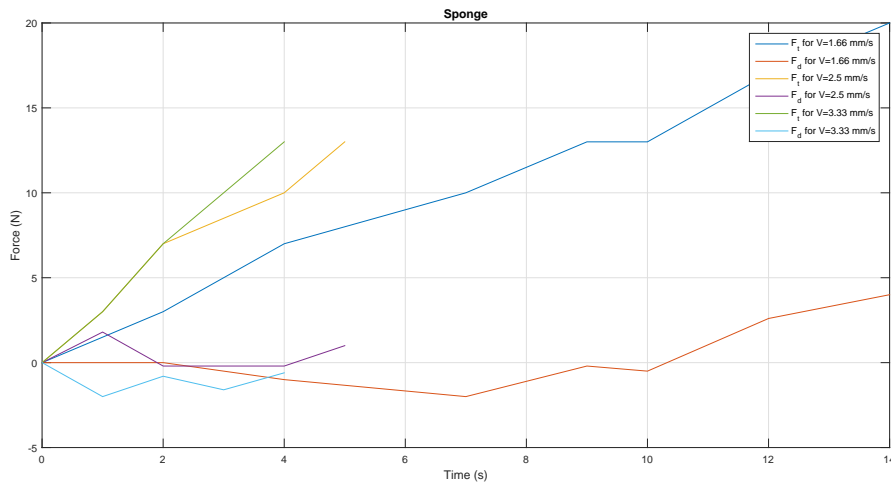
Figure 7.5: Total force F_t and damping force F_d for the 3 applied velocities, sponge environment

The damping coefficient of the environment, B_e, is found by averaging the damping force for one velocity, and divide it by the the corresponding velocity because collected data didn't reflect constant force F_d. The first velocity, $1.66\,\mathrm{mm/s}$ is used for this purpose. The stiffness and damping of the stress ball and sponge were found to be:

Environment	Stiffness (N/mm)	Damping (N.s/mm)
Stress ball	1.2266	0.3414
Sponge	0.7895	0.2184

Table 7.1: Stiffness and damping of each operating environment

7.1 Simulation Results

7.1.1 First simulation: Slave actuator facing a stress ball

In the first simulation, the system is tested against a stress ball facing the slave actuator with the values of stiffness and damping as given in table (7.1). The applied force is a constant $10\,\mathrm{N}$ force. Results for the three controllers are shown in figures (7.6),(7.7) and (7.8).

Figure 7.6: Master and slave positions of the teleoperator with the proportional controller operating against the stress ball

Figure 7.7: Master and slave positions of the teleoperator with the lead compensator controller operating against the stress ball

Figure 7.8: Master and slave positions of the teleoperator with the adaptive controller operating against the stress ball

43

The errors of the three controllers when the system is operating against the stress ball are shown in figure (7.9).
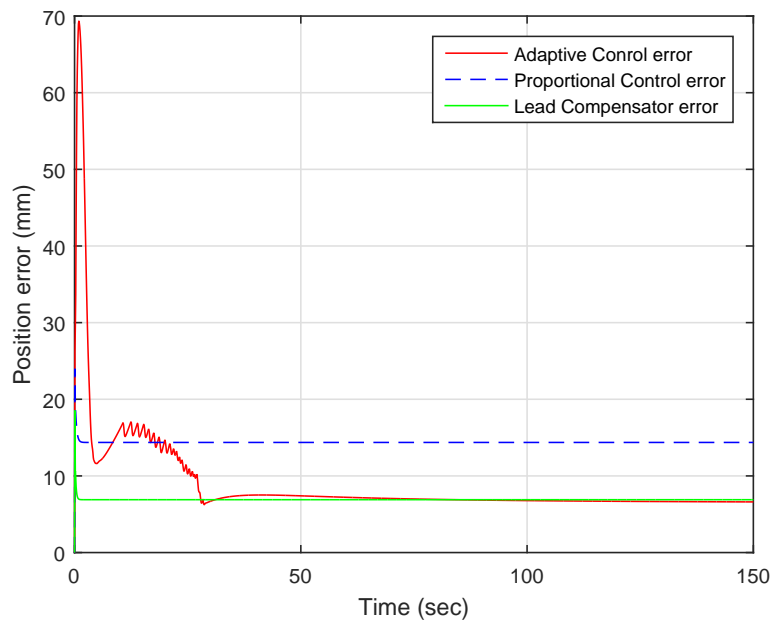
Figure 7.9: The error between master and slave positions of the three controllers for the first test

The advantage of adaptive over both lead compensator and proportional control is seen in terms of smaller error between master and slave pistons positions.

7.1.2 Second simulation: Slave actuator facing a sponge

In the second simulation, the system is tested against a sponge facing the slave actuator with the values of stiffness and damping as given in table (7.1). The applied force is a constant $10\,\mathrm{N}$ force. Results for the three controllers are shown in figures (7.10),(7.11) and (7.12). The errors of the three controllers when the system is operating against the sponge are shown in figure (7.13).
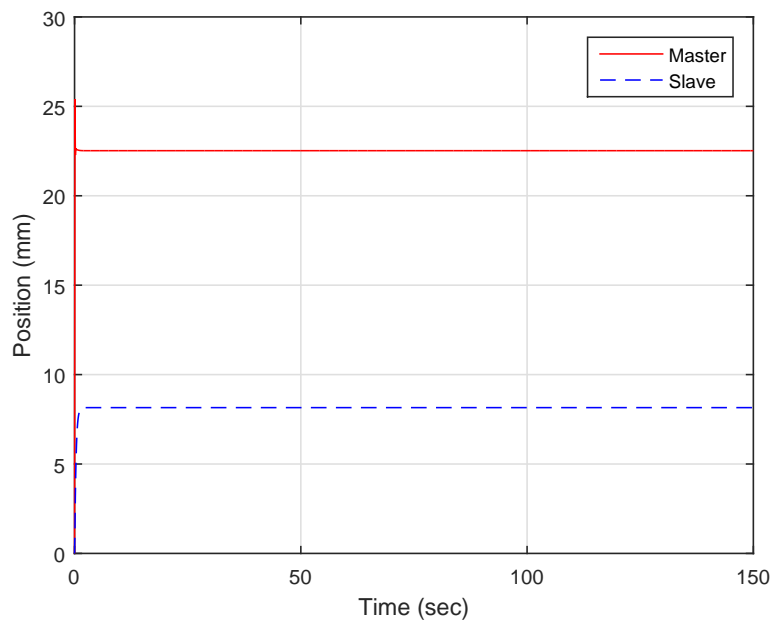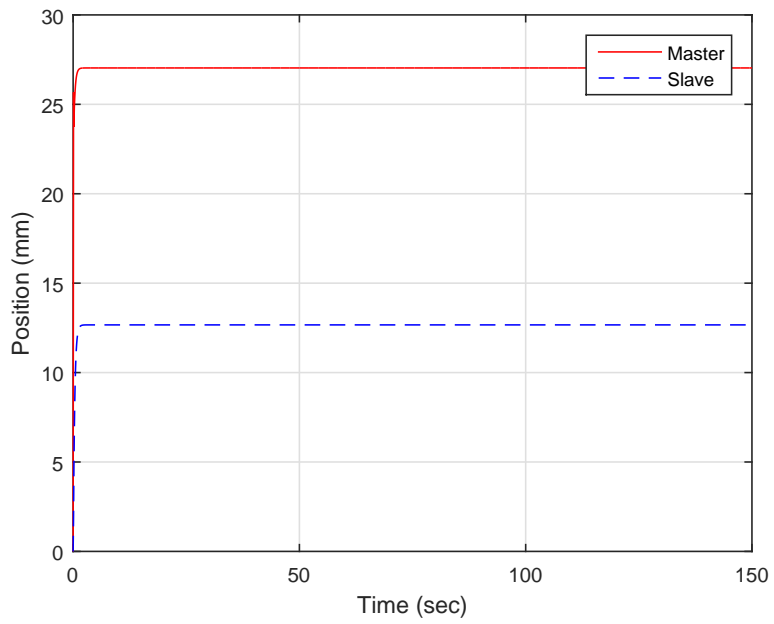
Figure 7.10: Master and slave positions of the teleoperator with the proportional controller operating against the sponge
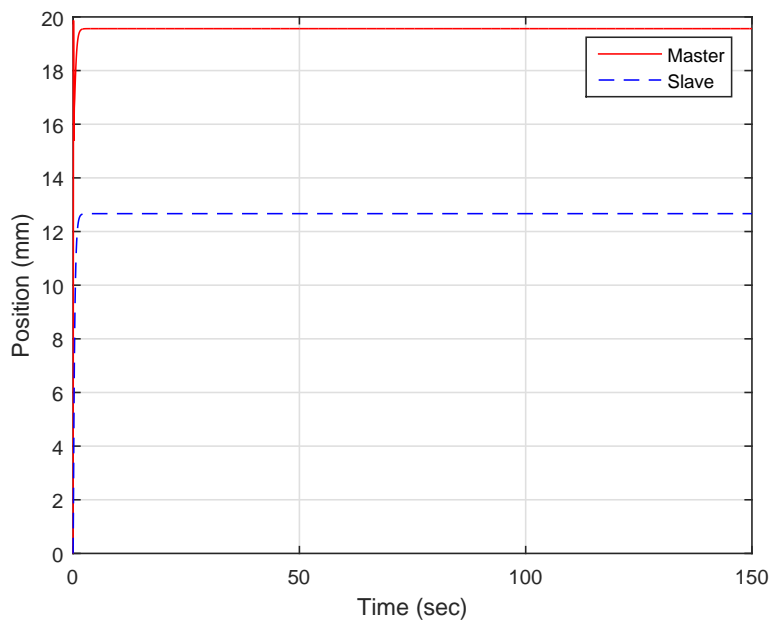
Figure 7.11: Master and slave positions of the teleoperator with the lead compensator controller operating against the sponge

45
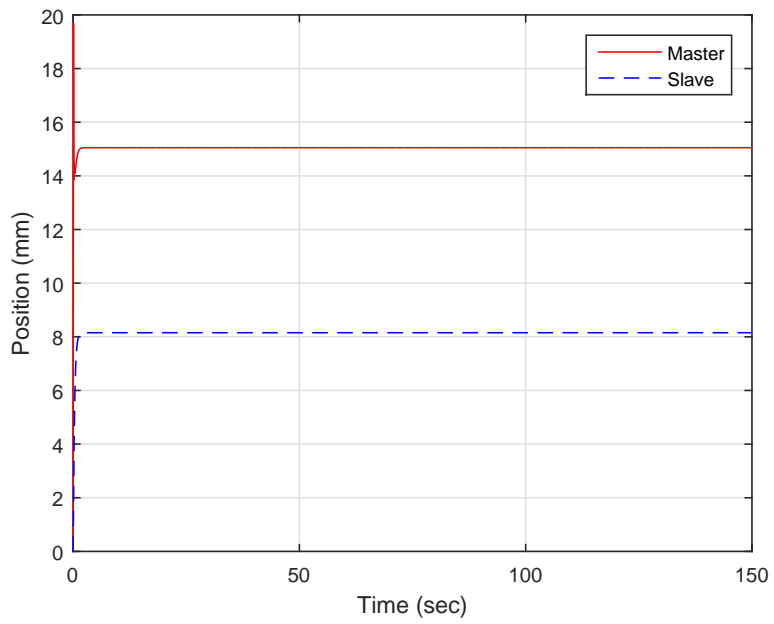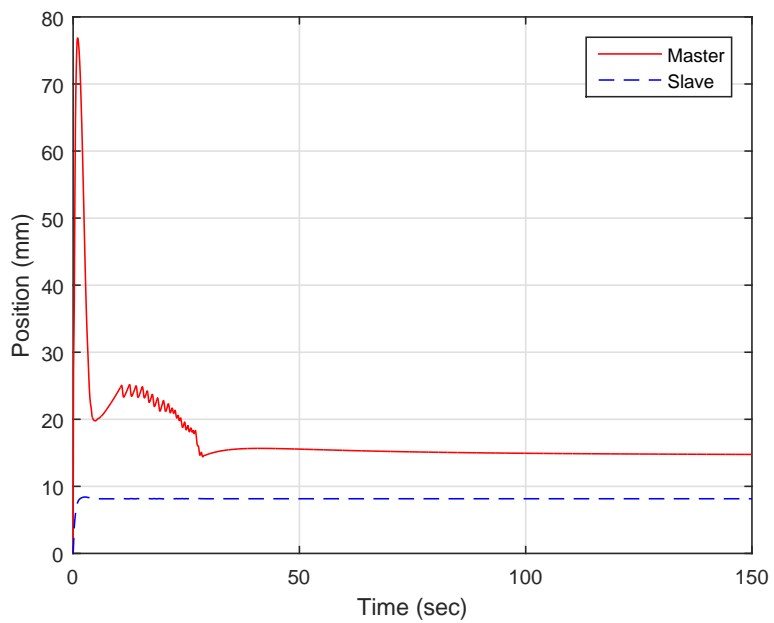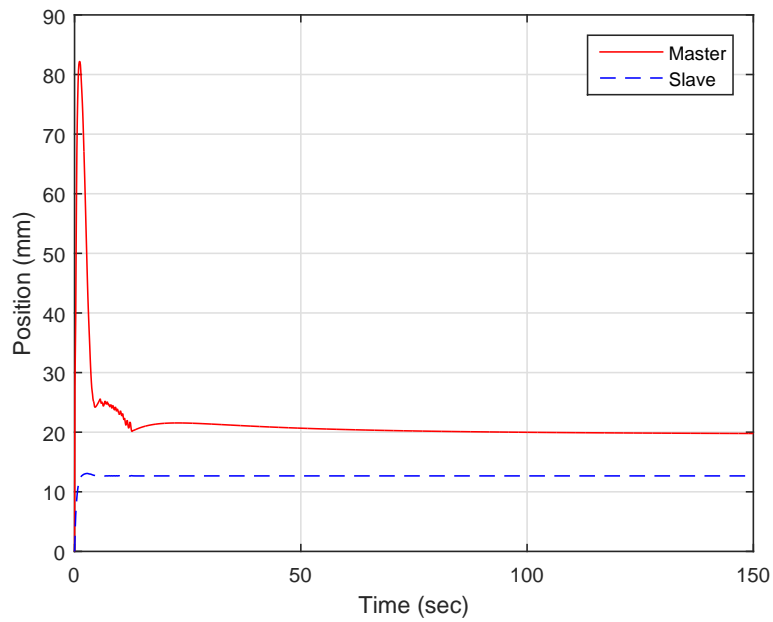
Figure 7.12: Master and slave positions of the teleoperator with the adaptive controller operating against the sponge
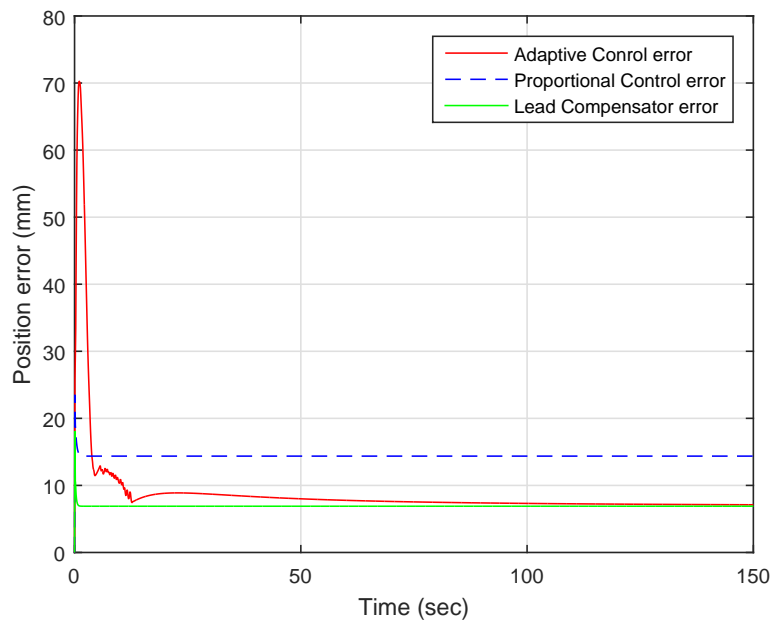
Figure 7.13: The error between master and slave positions for the three controllers for the second test

In this experiment also, the adaptive controller presented better results than both

linear controllers in terms of minimal error when operating in contact with each of the two environments.

7.2 Experimental Results

This section presents the experimental results of the system operating in 3 different environments facing the slave actuator: stress ball, sponge and a stone. In each case the operator applied a constant force forward, the actuator first is free to move, the slave actuator is facing nothing, then it reaches the specified environment, penetrates to a certain thickness then the operator suddenly removes his/her hand to check system performance due to sudden change in the operator's side force. The test rig used in the experiments in shown in figure (7.14).
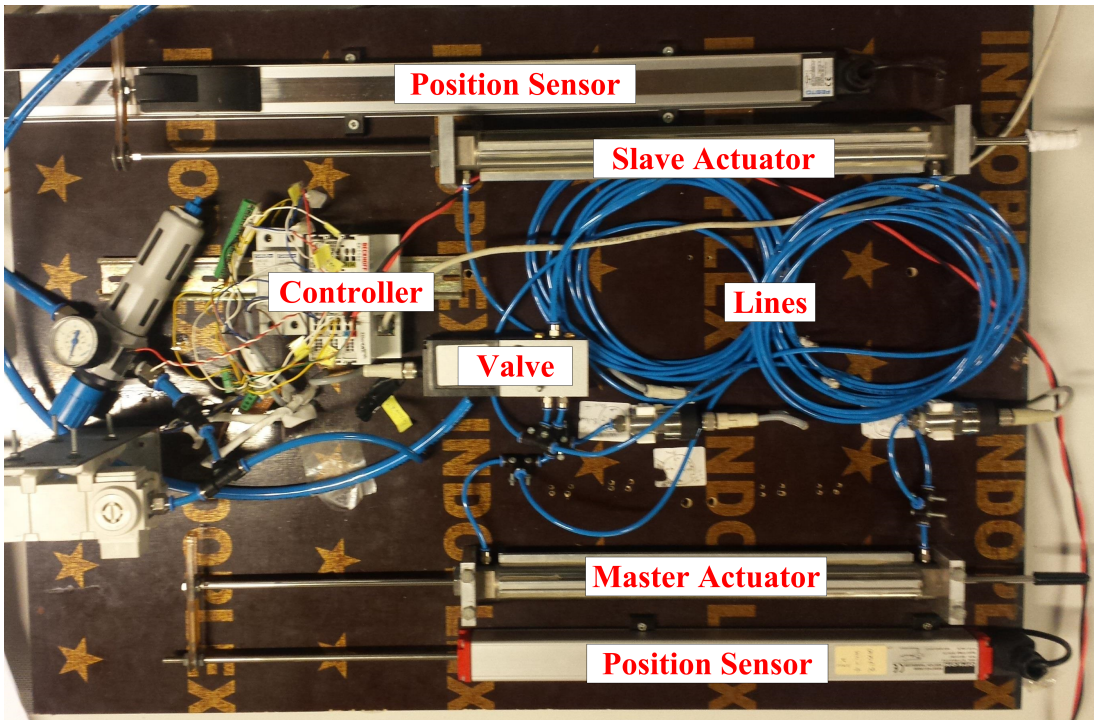
Figure 7.14: The test rig used in experiment, showing its different components

7.2.1 First experiment: Slave actuator facing a stress ball

In the first experiment, the system is tested against a stress ball facing the slave actuator as shown in figure (7.15). Results for the three controllers are shown in figures (7.16), (7.17) and (7.18). In each figure, the upper plot represents the position error between master and slave actuators, the middle plot represents the valve voltage input and the lower plot represents both master and slave pistons positions.

47
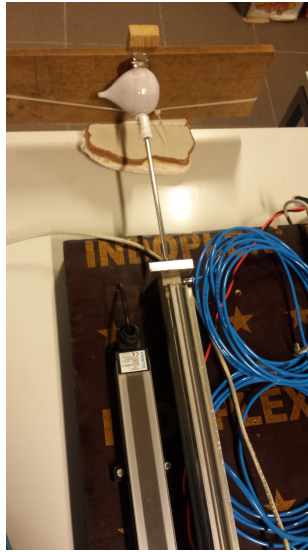
Figure 7.15: Testing the teleoperator facing the stress ball

Figure 7.16: Proportional Controller performance when the slave actuator is facing a stress ball

Figure 7.17: Lead compensator controller performance when the slave actuator is facing a stress ball

Figure 7.18: Adaptive controller performance when the slave actuator is facing a stress ball

All three controllers have additional error when contact started with the stress ball,

49

the proportional controller has increasing error with the increase of penetration depth. The lead compensator has smaller increase in error than the proportional control, while the adaptive control has sudden increase in error then adaptation in one second. After the sudden release of the operator hand, both proportional controller and lead compensator required around 4 seconds to take the error to zero, while adaptive controller required less than one second.

7.2.2 Second experiment: Slave actuator facing a sponge

In the second experiment, the system is tested against a sponge facing the slave actuator as shown in figure (7.19).
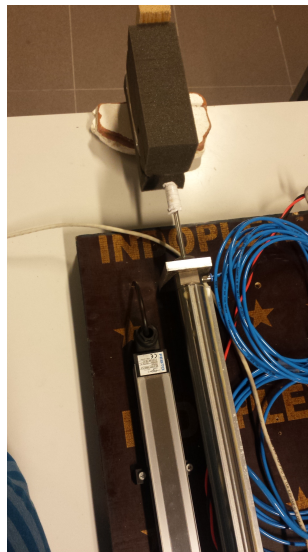
Figure 7.19: Testing the teleoperator facing the sponge

Results for the three controllers are shown in figures (7.20), (7.21) and (7.22).
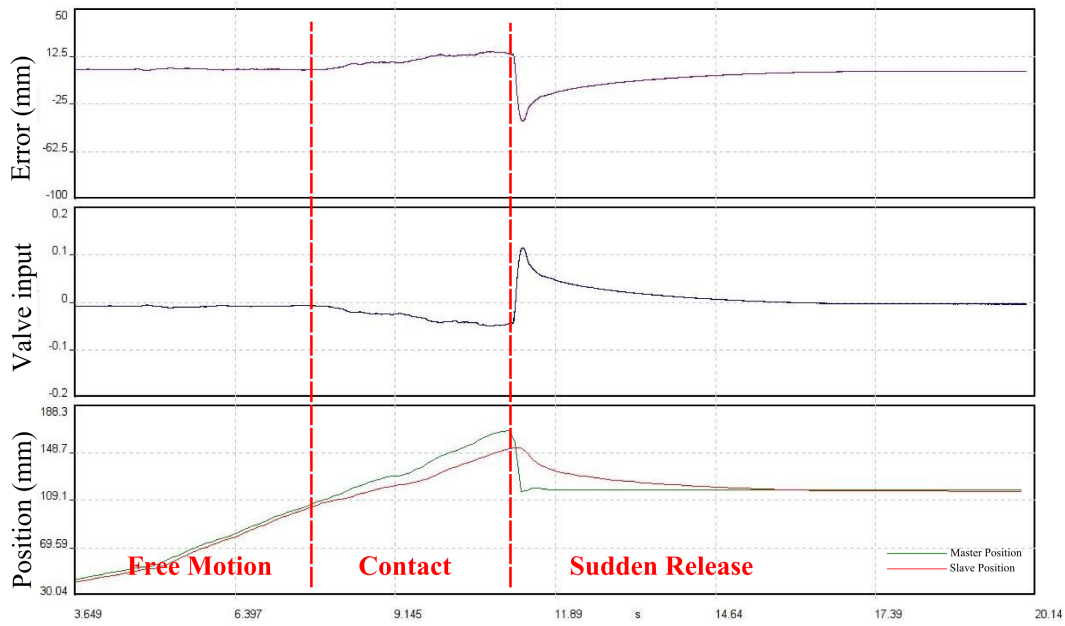
Figure 7.20: Proportional Controller performance when the slave actuator is facing a sponge
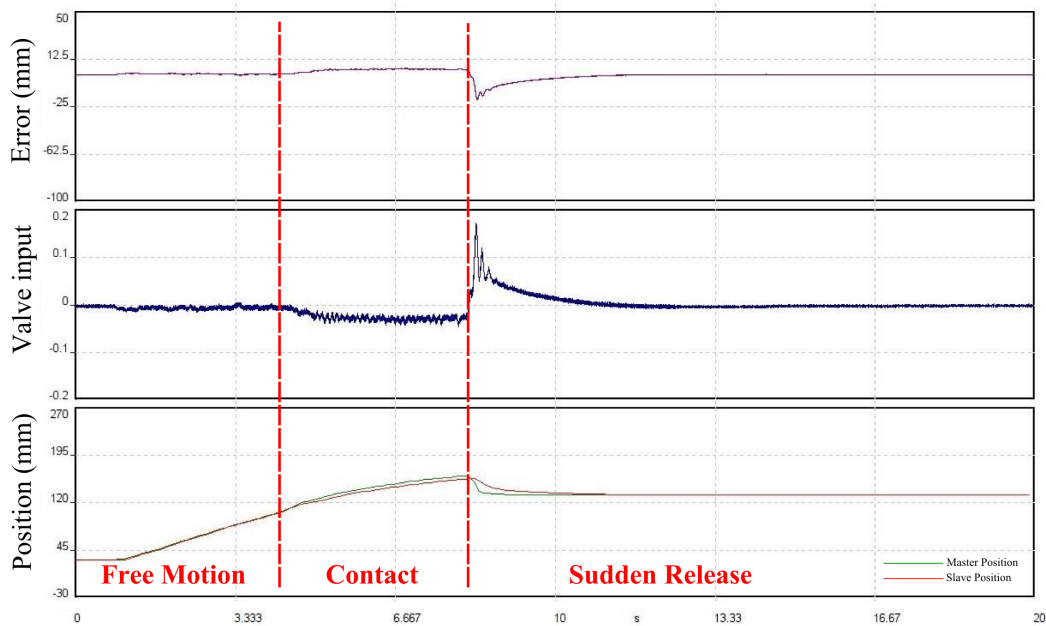
Figure 7.21: Lead compensator controller performance when the slave actuator is facing a sponge
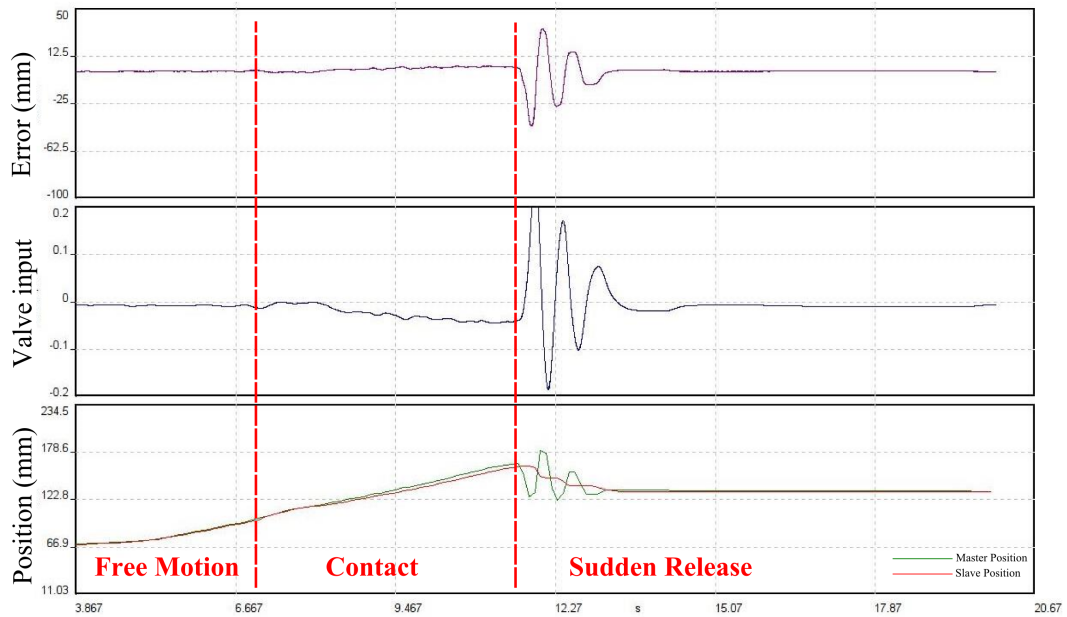
Figure 7.22: Adaptive controller performance when the slave actuator is facing a sponge

In the case of sponge, the error after the contact of the slave actuator with the sponge is significantly larger in the case of proportional controller as can be seen in figure (7.20), lead compensator allowed penetration with smaller increasing error while in the case of adaptive controller the error is negligible during the penetration. The sudden release error convergence in the adaptive contoller case is also faster than both proportional controller and lead compensator with overshoot.

7.2.3 Third experiment: Slave actuator facing a stone

In the third experiment, the system is tested against a stone facing the slave actuator as shown in figure (7.23).
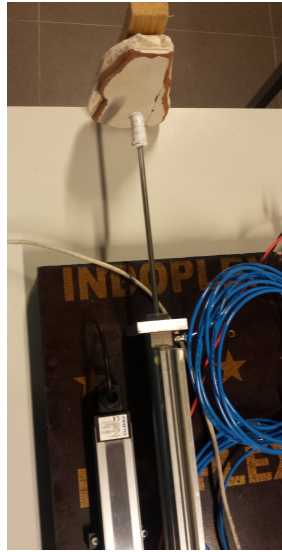
Figure 7.23: Testing the teleoperator facing the stone

The operator moved the piston first where the slave actuator is free to move, after it reached the stone an added force is exerted against the stone for some time then the operator's hand is suddenly released. Results for the three controllers are shown in figures (7.24), (7.25) and (7.26).
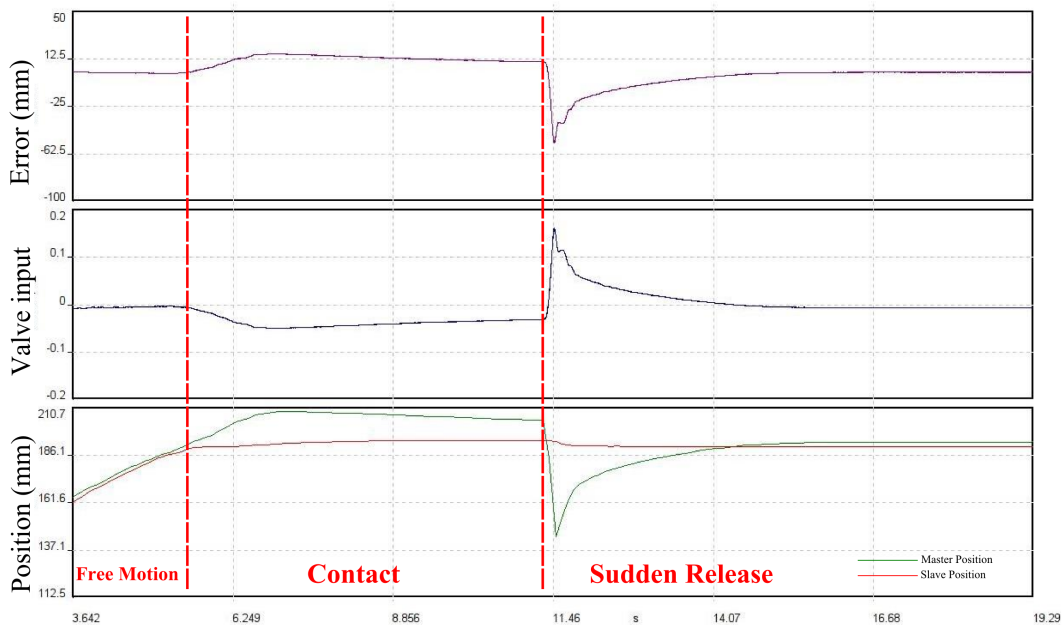
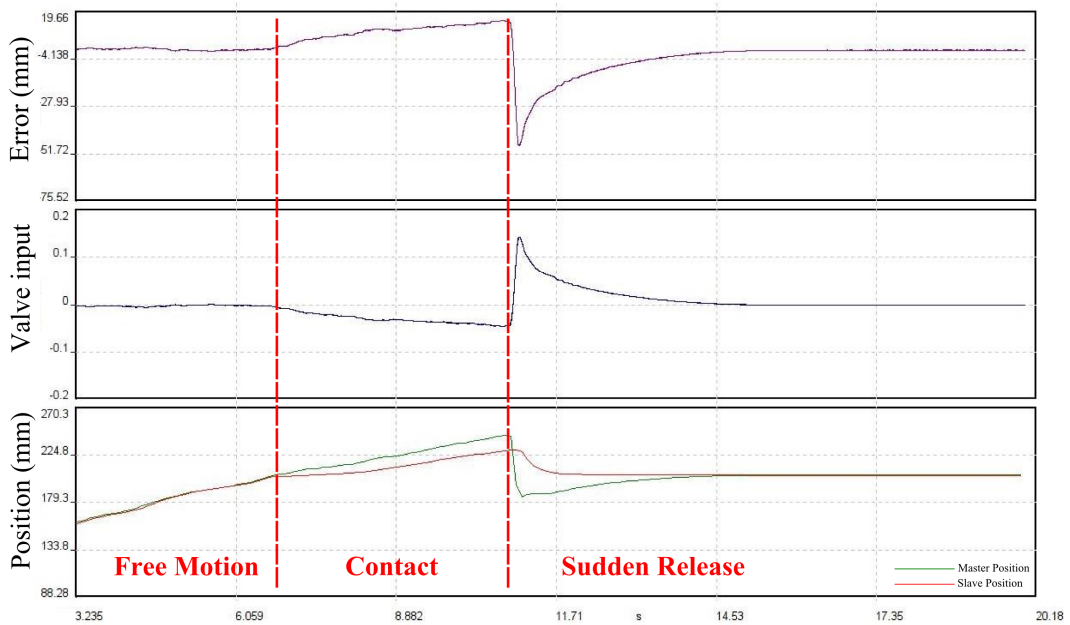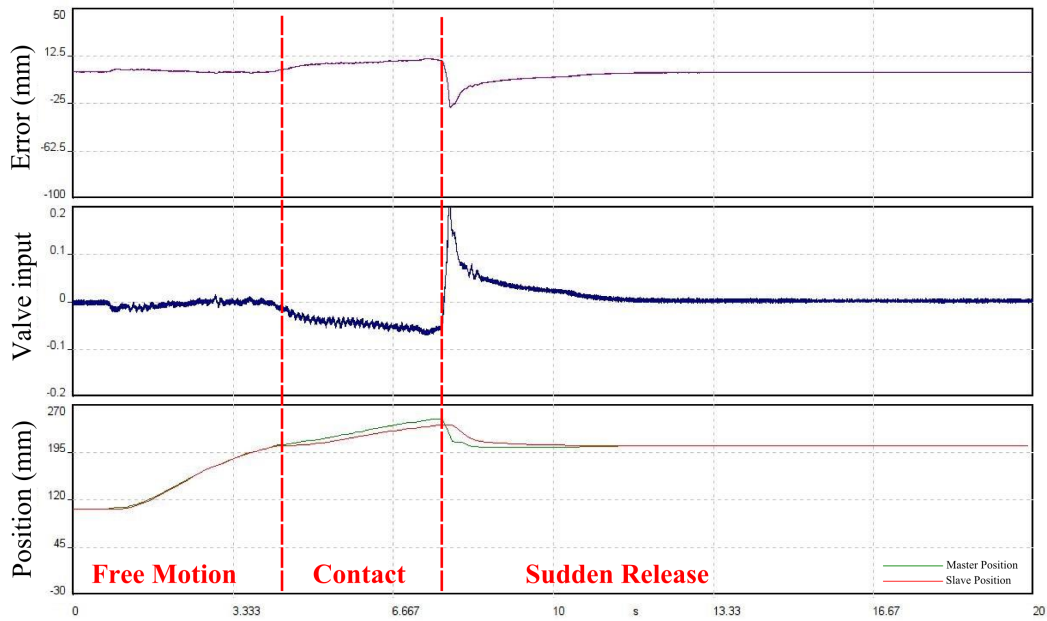Figure 7.24: Proportional Controller performance when the slave actuator is facing a stone
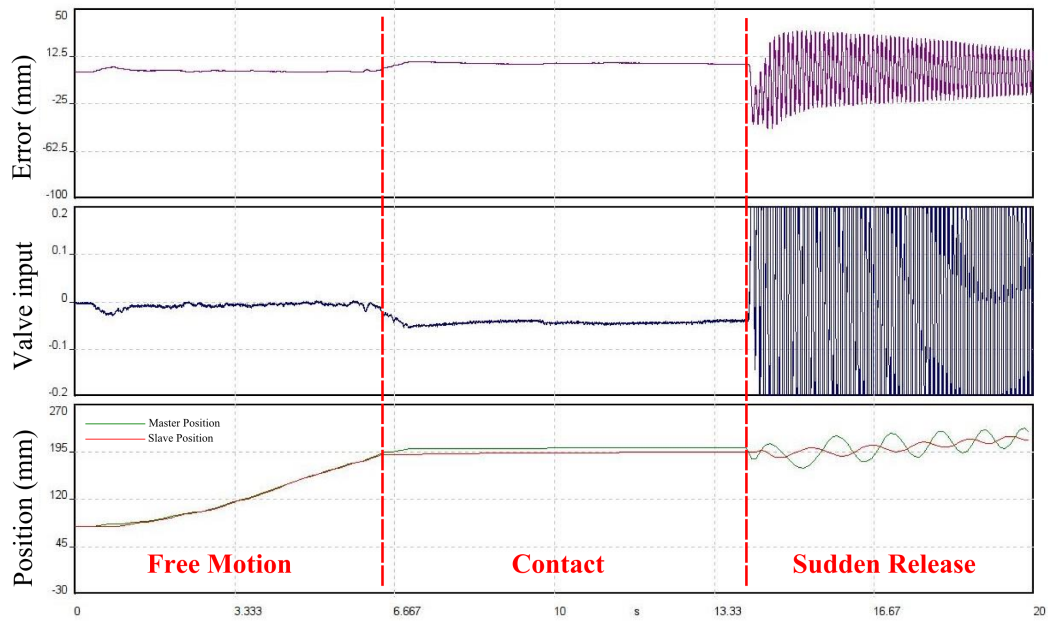
Figure 7.25: Lead compensator controller performance when the slave actuator is facing a stone
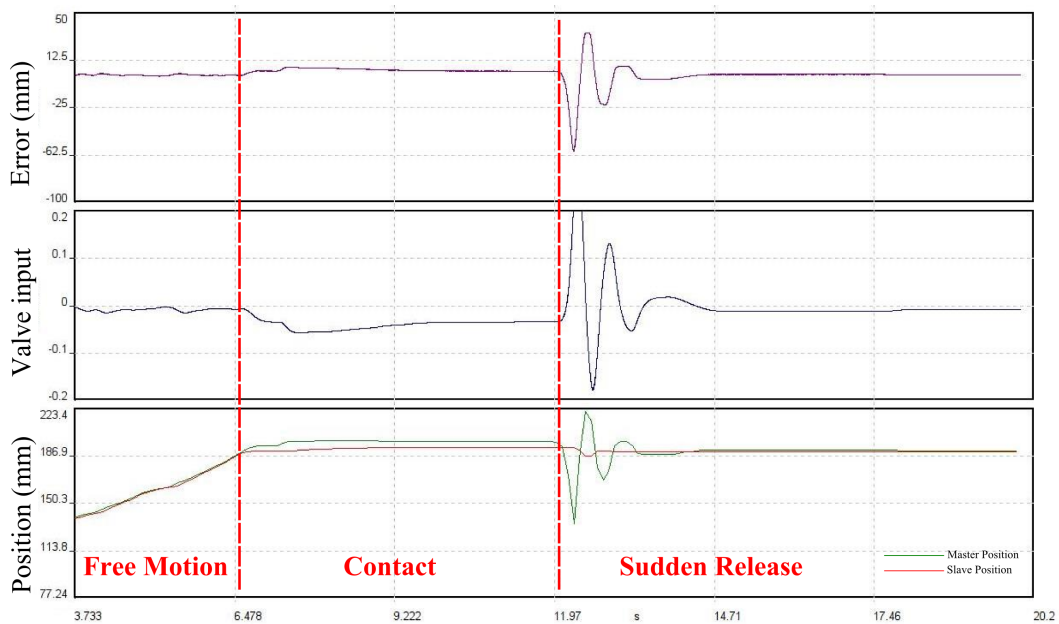
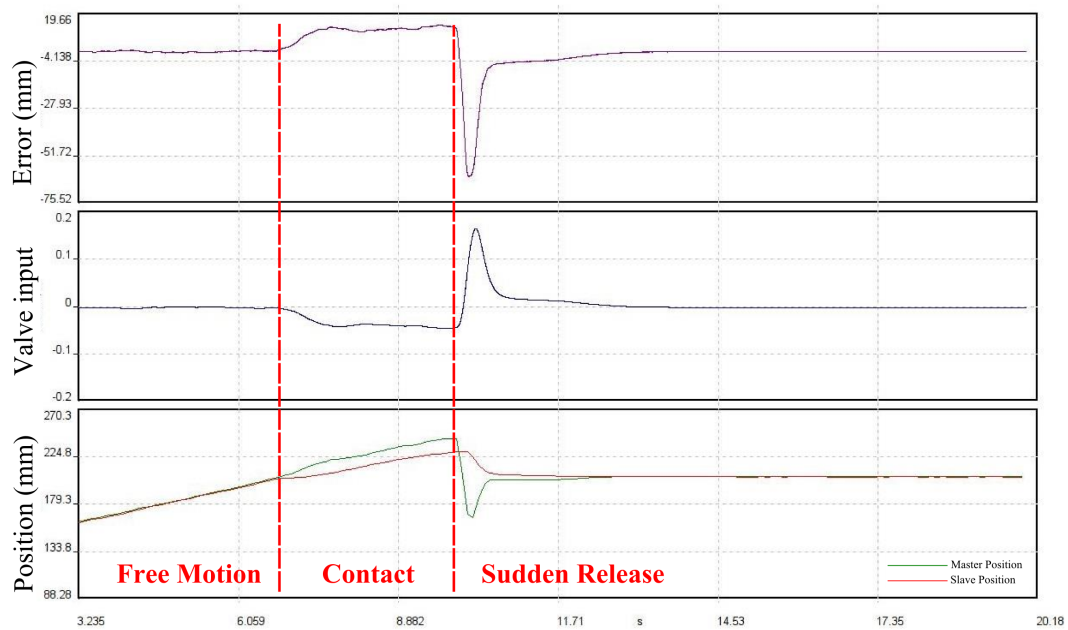Figure 7.26: Adaptive controller performance when the slave actuator is facing a stone

The error between the master and slave actuator positions in the proportional controller case is larger than the adaptive controller case when the contact occured with

the stone, and after the sudden release also the adaptive is faster to converge the error to zero with overshoot. The lead compensator presented smaller error when contact was occuring with the stone compared to the proportional controller, but the sudden release of the operator's hand made the system unstable, the instability is caused by limit cycles, the valve spool position is limited and the lead compensator has a high bandwidth which causes instability in some situations. Another very important notice regarding the lead compensator is that the voltage input of the valve is noisy in all the tested situations: free movement, contact (with stress ball, sponge or stone) or sudden release of the actuator by the human operator, which can dicrease valve life time and cause corrosion of the inner spool, while proportional and adaptive control provide smoother voltage signal.

7.3   Transparency Assessment

This section presents transparency assessment of both adaptive and proportional controllers when the system is operating against the stress ball and the sponge.

7.3.1   Transparency assessment of the system with the stress ball

The transparency ratio is given by equation (1.2). The teleoperator impedance Z_t using the adaptive controller is computed with equation (1.3), results are shown in table (7.2). The stress ball impedance, Z_e is found by plotting the body plot of its model

ω	$0.1\,\mathrm{rad/s}$	$0.3\,\mathrm{rad/s}$	$0.4\,\mathrm{rad/s}$	$0.5\,\mathrm{rad/s}$	$1\,\mathrm{rad/s}$
Magnitude of $Z_t(\,\mathrm{N.s/mm})$	7.8	1.971	1.3447	0.9841	1.11
Phase of $Z_t(\,\mathrm{deg})$	89.0976	88.6233	86.2166	88.1656	74.5223

Table 7.2: Magnitude and phase shift of the Z_t using the adaptive controller, stress ball case

with previously mentioned values of stiffness and damping, values of magnitude and phase at the four given frequencies are given in table (7.3). The transparency ratio of

ω	$0.1\,\mathrm{rad/s}$	$0.3\,\mathrm{rad/s}$	$0.4\,\mathrm{rad/s}$	$0.5\,\mathrm{rad/s}$	$1\,\mathrm{rad/s}$
Magnitude of $Z_e(\,\mathrm{N.s/mm})$	12.0226	4.0272	3.1623	2.5148	1.2735
Phase of $Z_e(\,\mathrm{deg})$	-88.3	-85.1	-83.8	-82.2	-74.4

Table 7.3: Magnitude and phase shift of the stress ball impedance

the system using the proportional controller is found from linear analysis as done in chapter (4). The transparency ratio of the system operating against the stress ball, for both adaptive and proportional controller is plotted in figure (7.27).
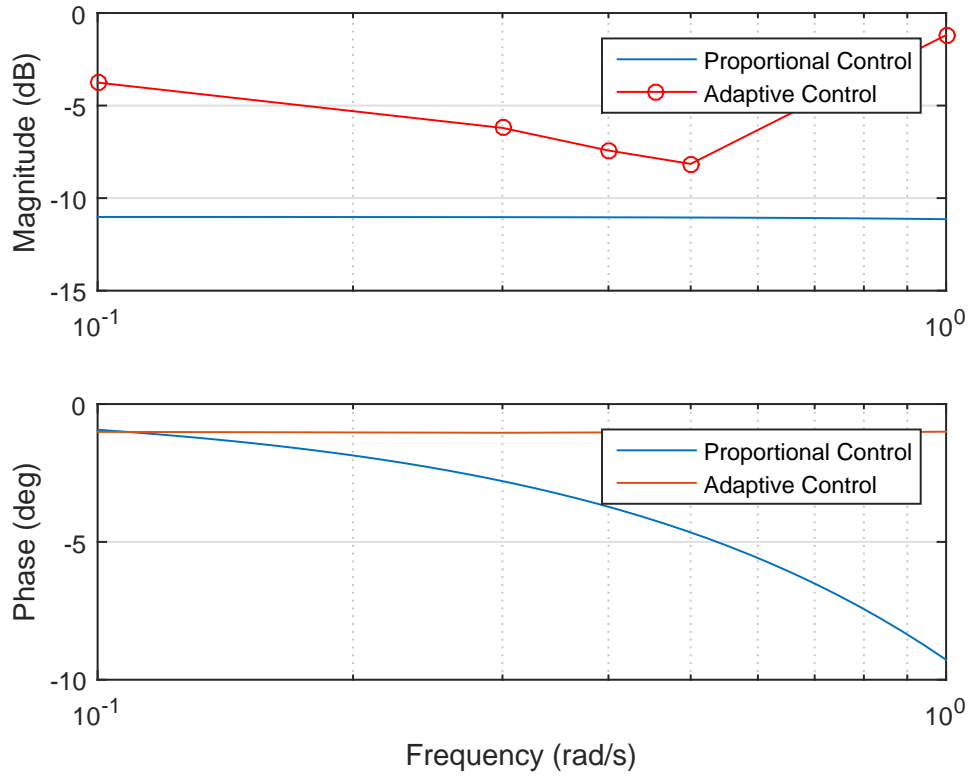
Figure 7.27: Bode Plot of transparency ratio of the system with the stress ball environment

7.3.2 Transparency assessment of the system with the sponge

The teleoperator impedance Z_t using the adaptive controller is computed with equation (1.3), results are shown in table (7.4). The sponge impedance, Z_e is found by plotting

ω	$0.1\,\mathrm{rad/s}$	$0.3\,\mathrm{rad/s}$	$0.4\,\mathrm{rad/s}$	$0.5\,\mathrm{rad/s}$	$1\,\mathrm{rad/s}$
Magnitude of $Z_t(\mathrm{N.s/mm})$	4.795	1.6447	1.4706	1.4286	0.5869
Phase of $Z_t(\deg)$	88.9682	89.0842	87.1338	80.5414	85.9873

Table 7.4: Magnitude and phase shift of Z_t using the adaptive controller, sponge case

the body plot of its model with previously mentioned values of stiffness and damping, values of magnitude and phase at the four given frequencies are given in table (7.5). The transparency ratio of the system using the proportional controller is found from linear analysis as done in chapter (4). The transparency ratio of the system operating against the sponge, for both adaptive and proportional controller is plotted in figure (7.28).

ω	$0.1\,\mathrm{rad/s}$	$0.3\,\mathrm{rad/s}$	$0.4\,\mathrm{rad/s}$	$0.5\,\mathrm{rad/s}$	$1\,\mathrm{rad/s}$
Magnitude of $Z_e(\,\mathrm{N.s/mm})$	7.4131	2.5793	2.0417	1.6181	0.8194
Phase of $Z_e(\,\mathrm{deg})$	-88.3	-85.1	-83.9	-82.2	-74.5

Table 7.5: Magnitude and phase shift of the sponge impedance
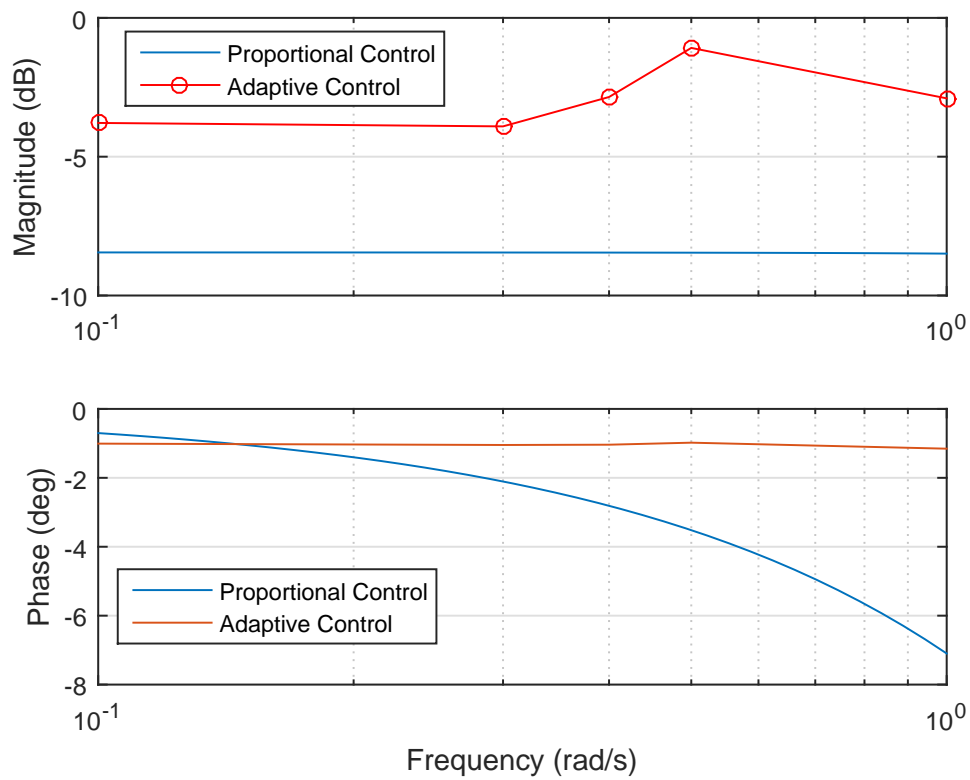
Figure 7.28: Bode Plot of transparency ratio of the system with the stress ball environment

Chapter 8

Conclusion

Proportional and lead compensator controllers with pressure feedback were designed to control the proposed teleoperator. The slave actuator was capable of following the master when controller parameters are chosen correctly, and it was shown that lead compensator has advantage over the proportional controller. Since the teleoperator is to be implemented under live MRI imaging, where parameters of environment facing the slave actuator and human operator arm are varying, it was shown that both proportional and lead compensator controllers were not capable of properly adapting to this change.

The proposed adaptive controller is tested under different operating conditions, both in simulation and on the test rig. Tests were conducted with different environments facing the slave actuator, different user behavior, and it presented smaller error in contact with different physical environments than linear controllers, and faster adaptation when sudden action occurs in both sides of the teleoperator: human operator side and physical environment side. As a conclusion, improving the controller is a good approach to improve teleoperator performance, using a nonlinear controller that can change its gains based on the change in system parameters is a suggested solution to be used in case of teleoperators operating in variable conditions. As future work, Model Reference Adaptive Control (MRAC) can be applied to the system, in addition to adaptation to any change in system parameters, this controller guarantees stability of the system.

Appendix A

Abbreviations

$x_{mE} = \frac{l_{cyl}}{2}$.

$P_{atm} = 1.013$.

$P_{m1E} = \frac{-\sqrt{P_{atm}^2 b_v^2 - 2P_{atm}^2 b_v + 2P_{atm}^2 - 2P_{atm}P_s b_v^2 + 5P_s^2 b_v^2 - 6P_s^2 b_v + 2P_s^2)}}{2(b_v - 1)}$
$- \frac{P_s b_v - P_{atm} b_v}{2(b_v - 1)}$.

$P_{m2E} = P_{m1E}$.

$x_{sE} = \frac{l_{cyl}}{2}$.

$P_{s1E} = P_{m1E}$.

$P_{s2E} = P_{m1E}$.

$c_1 = \frac{RT}{V_{md} + x_{mE}\frac{A_p}{10^6}}$.

$c_2 = \frac{P_{m1E}A_p}{10^6 V_{md} + x_{mE}A_p}$.

$c_3 = \frac{RT}{V_{md} + (l_{cyl} - x_{mE})\frac{A_p}{10^6}}$.

$c_4 = \frac{P_{m2E}A_p}{10^6 V_{md} + (l_{cyl} - x_{mE})A_p}$.

$c_5 = \frac{RT}{V_{sd} + x_{sE}\frac{A_p}{10^6}}$.

$c_6 = \frac{P_{s1E}A_p}{10^6 V_{sd} + x_{sE}A_p}$.

$c_7 = \frac{RT}{V_{sd} + (l_{cyl} - x_{sE})\frac{A_p}{10^6}}$.

$c_8 = \frac{P_{s2E}A_p}{10^6 V_{sd} + (l_{cyl} - x_{sE})A_p}$.

$c_9 = C_v \rho_0 P_s \sqrt{1 - \left(\frac{\frac{P_{m1E}}{P_s} - b_v}{1 - b_v}\right)^2}$.

$c_{10} = C_v \rho_0 P_s \sqrt{1 - \left(\frac{\frac{P_{m2E}}{P_s} - b_v}{1 - b_v}\right)^2}$.

$c_{11} = \frac{100 A_t}{L_t}$.

$c_{12} = \frac{\frac{10^6 RT}{A_t}}{L_t}$.

$c_{22} = \frac{32\mu.10^6}{\rho_0 D_t^2}$

Appendix B

Nomenclature

Table B.1: Nomenclature

Symbol	Comment	Value	Unit
x_h	Hand position		m
x_m	Master cylinder position		m
F_h	Hand force		N
m_p	Mass of the piston	0.2546	kg
β	Viscous friction of the cylinders	0.0116	$N.s/mm$
$P_{m1,2}$	Pressures across chambers 1,2 of the master cylinder		Pa
A_p	Piston area	420.7201	mm^2
x_s	Position of the slave cylinder		m
$P_{s1,2}$	Pressure across chambers 1,2 of the slave cylinder		bar
P_{m1}	Pressure in chamber 1 of the master		Pa
R	Ideal gas constant	2.87	$bar.L/Kg.K$
T	Gas temperature	293.15	$K°$
V_{i1}	Volume of chamber 1 of master		m^3
$\dot{m}_{1m}$	Mass flow rate in chamber 1		kg/s
V_{1m}	Dead volume for the master cylinder	0.002	m^3
l_{cyl}	Total cylinder length	275	mm
$x_{v1,2}$	Relative spool position of the valve 1,2		m
c	Sonic conductance given by the valve manufacturer	0.45	$L/bar.s$
ρ_0	Density of air at reference conditions	0.0012	kg/L
P_{u1}	Upstream pressure of valve 1		Pa
T_0	Temperature of air at reference conditions		$K°$
$T_{1,2}$	Upstream temperature of valve 2		$K°$
P_{d1}	Downstream pressure of valve 1		Pa
b	Critical pressure ratio given by the valve manufacturer	0.21	
K_v	Electromechanical valve gain	0.2	$1/V$
$u_{1,2}$	Input voltage to the valve 1,2		V
v	Air kinematic viscosity	$1.568 \cdot 10^{-5}$	m^2/s
A	Cross sectional area of the pneumatic line	12.5664	mm^2
L	Pneumatic line length	5	m
μ	Dynamic viscosity of air	1.8127×10^{-8}	$kg/mm.s$
$\bar{w}$	Mean air velocity through the pneumatic line		m/s^2
D	Tube diameter	4	mm
D_p	Piston diameter	11.57	mm
P_s	Pressure supply to the valves	3	bar
P_T	Atmospheric pressure	1	bar

Bibliography

[1] T. Sheridan, "Telerobotics," *Automatica*, vol. 25, no. 4, pp. 487–507, 1989.

[2] P. F. Hokayem and M. W. Spong, "Bilateral teleoperation: An historical survey," *Automatica*, vol. 42, no. 12, pp. 2035–2057, 2006.

[3] M. Zhu and S. E. Salcudean, "Achieving transparency for teleoperator system under position and rate control," pp. 7–12, 1995.

[4] A. Jazayeri and M. Tavakoli, "Revisiting llewellyns absolute stability criterion for bilateral teleoperation systems under non-passive operator or environment," in *2012 IEEE/RSJ International Conference on Intelligent Robots and Systems*, pp. 70–75, October 7-12 2012.

[5] D. Lawrence, "Stability and transparency in bilateral teleoperation," *Robotics and Automation, IEEE Transactions*, vol. 9, no. 5, pp. 624–637, 1993.

[6] A. Elmasry and M. Liermann, "Passive pneumatic teleoperation system," in *Proceedings of the ASME/BATH 2013 Symposium on Fluid Power & Motion Control FPMC2013*, 2013.

[7] A. Albakri, C. Liu, and P. Poignet, "Stability and performance analysis of three-channel teleoperation control architectures for medical applications," in *2013 IEEE/RSJ International Conference on Intelligent Robots and Systems*, pp. 456–462, 2013.

[8] C. Pacchierotti, A. Tirmizi, G. Bianchini, and D. Prattichizzo, "Improving transparency in passive teleoperation by combining cutaneous and kinesthetic force feedback," in *2013 IEEE/RSJ International Conference on Intelligent Robots and Systems*, (Tokyo, Japan), pp. 4958–4963, 2013.

[9] O. Gerovich, P. Marayong, and A. Okamura, "The effect of visual and haptic feedback on computer-assisted needle insertion," *Computer Aided Surgery,*, vol. 9, no. 6, pp. 243–249, 2004.

[10] S. Misra and A. Okamura, "Environment parameter estimation during bilateral telemanipulation," in *Symposium on Haptic Interfaces for Virtual Environment and Teleoperator Systems 2006* (A. Editor, ed.), pp. 301–307, 2006.

[11] E. T.Wolbrecht, D. J. Reinkensmeyer, and J. E. Bobrow, "Pneumatic control of robots for rehabilitation," *The International Journal of Robotics Research*, pp. 23–38, May 2009.

[12] G. S. Fischer, I. Iordachita, C. Csoma, J. Tokuda, S. P. DiMaio, C. M. Tempany, N. Hata, and G. Fichtinger, "Mri-compatible pneumatic robot for transperineal prostate needle placement," *IEEE/ASME Trans*, vol. 13, pp. 295 – 305, June 2008.

[13] M. Li, A. Kapoor, D. Mazilu, and K. A. Horvath, "Pneumatic actuated robotic assistant system for aortic valve replacement under mri guidance," *IEEE Transactions on Biomedical engineering*, vol. 58, pp. 443 – 451, February 2001.

[14] P. Beater, *Pneumatic drives: system design, modeling and control*. Springer, 2007.

[15] S. Krichel and O. Sawodny, "Dynamic modeling of pneumatic transmission lines in matlab/simulink," in *Proceedings of Fluid Power and Mechatronics (FPM 2011) International Conference*, pp. 24–29, 2011.

[16] K. Ogata, *Modern Control Engineering*. Prentice Hall, 2010.

[17] K. Astrom and B. Wittenmark, *Adaptive Control*. NY: Dover Mineola, 2008.

[18] K. Astrom and B. Wittenmark, *Computer Controlled Systems*. Prentice Hall.